Generation of the Mt Kinabalu granite by crustal contamination of intraplate magma modelled by Equilibrated Major Element Assimilation with Fractional Crystallisation (EME-AFC)

Burton-Johnson, A[a*], Macpherson, C.G.[b], Ottley, C.J.[b], Nowell, G.M.[b], and Boyce, A.J.[c]

[a]British Antarctic Survey, High Cross, Madingley Road, Cambridge, CB3 0ET, UK

[b]Department of Earth Sciences, University of Durham, Durham, DH1 3LE, UK

[c]Scottish Universities Environmental Research Centre, East Kilbride, G75 0QF, UK

*Author for correspondence

e-mail: alerto@bas.ac.uk

Tel. +44 (0)1223 221284

ABSTRACT

We present new geochemical data for the composite units of the Mount Kinabalu granitoid intrusion of Borneo and explore discrimination between crustal- and mantle-derived granitic magmas. The geochemical data demonstrate that the units making up this composite intrusion became more potassic through time. This was accompanied by an evolution of isotope ratios from a continental-affinity towards a slightly more mantle-affinity ($^{87}Sr/^{86}Sr_i$ ~0.7078; $^{143}Nd/^{144}Nd_i$ ~0.51245; $^{206}Pb/^{204}Pb_i$ ~18.756 for the oldest unit compared to $^{87}Sr/^{86}Sr_i$ ~0.7065, $^{143}Nd/^{144}Nd_i$ ~0.51250 and $^{206}Pb/^{204}Pb_i$ ~18.721 for the younger units). Oxygen isotope ratios (calculated whole rock $\delta^{18}O$ of +6.5–9.3‰) do not show a clear trend with time. The isotopic data indicate that the magma cannot be the result only from fractional crystallisation of a mantle-derived magma. Alkali metal compositions show that crustal anatexis is also an unsuitable processes for genesis of the intrusion. The data indicate that the high-K units were generated by fractional crystallisation of a primary, mafic magma followed by assimilation of the partially melted sedimentary overburden. We present a new, Equilibrated Major Element – Assimilation with Fractional Crystallisation (EME-AFC) approach for simultaneously modelling the major element, trace element, and radiogenic and oxygen isotope compositions during such magmatic differentiation; addressing the lack of current AFC modelling approaches for felsic, amphibole- or biotite-bearing systems. We propose that Mt Kinabalu was generated through low degree melting of upwelling fertile metasomatised mantle driven by regional crustal extension in the Late Miocene.

KEY WORDS

Granite petrogenesis; Magma differentiation; AFC modelling; Oxygen isotopes; Borneo

INTRODUCTION

Granitic intrusions form the majority of the Earth's upper continental crust and are commonly associated with precious metal deposits. Understanding their emplacement mechanisms and structure in the crust has evolved from models of slow moving diapirs to rapid, often pulsed, dyke emplacement of laterally extensive laccoliths (e.g. Wiebe, 1988; Clemens and Mawer, 1992; McCaffrey and Petford, 1997; Cruden, 1998; Wiebe and Collins, 1998; Petford and Clemens, 2000; Petford *et al.*, 2000; Vigneresse and Clemens, 2000; de Saint-Blanquat *et al.*, 2006; Vigneresse, 2006; de Silva and Gosnold, 2007; Grocott *et al.*, 2009; Horsman *et al.*, 2009). However, the processes that generate granitic melts remain ambiguous and debated (e.g. de Fátima Bitencourt *et al.*, 2017; Jagoutz and Klein, 2018).

Three potential mechanisms for producing granitic melts are widely accepted: (i) fractionation of mafic mantle derived melts, (ii) crustal anatexis, and (iii) mixing of mantle and anatectic melts. Each of these have been proposed for different plutons worldwide (e.g. Bogaerts *et al.*, 2006; Jagoutz *et al.*, 2009; Clemens and Benn, 2010; Chappell and White, 2011; Leuthold *et al.*, 2012). Distinguishing between these processes remains contentious and a fundamental challenge in igneous petrogenesis, but one that is best tackled through a comprehensive geochemical approach.

In this paper we present new geochemical data for the Mt Kinabalu pluton of Sabah in Malaysian Borneo. This is an ideal target to study granite petrogenesis because it is composed of units that are mineralogically and geochemically distinct and have ages that are well constrained by both contact relationships and U-Pb zircon dating (Cottam *et al.,* 2010; Burton-Johnson *et al.,* 2017). We show that neither crustal anatexis nor fractionation of mantle melts without crustal involvement are suitable mechanisms to generate this body. Utilising a new geochemical modelling approach we show that the intrusion's granitic magma was produced by crustal contamination of mantle derived, intra-plate magma by Assimilation and Fractional Crystallisation (AFC) processes.

REGIONAL GEOLOGY

At 4095m elevation, Mt Kinabalu is the highest peak between the Himalayas and Papua New Guinea (Fig. 1a and 1b). The Mt Kinabalu pluton was emplaced in Sabah, NW Borneo during the late Miocene (Fig. 1c). The region has basement made up of four main components: Jurassic to Cretaceous mafic igneous rocks; Cretaceous radiolarian cherts; variably serpentinised peridotites; and Triassic to Cretaceous rocks, previously described as crystalline basement (Reinhard and Wenk, 1951; Dhonau and Hutchison, 1965; Koopmans, 1967; Kirk, 1968; Leong, 1974; Rangin *et al.*, 1990; Omang, 1993; Swauger *et al.*, 1995; Graves *et al.,* 2000; Hutchison, 2005). These are overlain by a thick cover sequence of predominantly deep-water turbidites and related deposits (Collenette, 1965; van Hattum *et al.,* 2013) of the Cretaceous to Eocene Rajang Group (Sapulut Formation) and the Eocene to Oligocene Crocker Group (including the Trusmadi, Crocker, and Temburong Formations.)

The basement and cover sequence were folded and faulted during Eocene and Oligocene deformation driven by the subduction of the proto-South China Sea beneath Borneo (Taylor & Hayes 1983; Rangin & Silver 1990; Tongkul 1991, 1994; Hall 1996; Hall & Wilson 2000; Hutchison 2000). The attenuated South China continental margin collided with northern Borneo in the Early Miocene (Hall and Wilson, 2000; Hutchison, 2000; Hall and Breitfeld, 2017) triggering the Sabah Orogeny (Hutchison, 1996). The Kinabalu granite was intruded, under extensional strain, into the central Crocker Mountains in the Late Miocene (7-8 Ma; Cottam *et al.*, 2010; Burton-Johnson *et al.*, 2017, 2019). The nearest contemporaneous granitic magmatism is the Capoas Granite (Fig. 1a), 600 km to the NE in Palawan (13.5 Ma, Suggate *et al.* 2013), although <5 Ma enriched basaltic to dacitic magmatism is recorded in Borneo on the Semporna Peninsula, and at Usun Apau and Linau Balui (Fig. 1a, Macpherson *et al.,* 2010; Cullen *et al.,* 2013).

Field relations of the Mt Kinabalu pluton

The Mt Kinabalu pluton was emplaced as six major granitic units (Fig. 1c, see Burton-Johnson *et al.*, 2017 for petrographic descriptions). Revised field relationships and U-Pb zircon ages have shown that the composite pluton was initially emplaced from the top down in a broadly laccolitic structure through upward deformation of the host rocks (Cottam *et al.,* 2010; Burton-Johnson *et al.,* 2017). Consequently, the oldest unit, the Alexandra Tonalite/Granodiorite (7.85 ±0.08 Ma), lies above subsequent, larger units of the Low's Granite (7.69 ±0.07 Ma) and the King Granite (7.46 ±0.08 Ma). The smaller, vertical, planar Donkey Granite (7.49 ±0.03 Ma) intruded the King Granite before the latter could fully crystallise, producing contacts

that vary between gradational and mingled. The final two porphyritic units (the Paka Porphyritic Granite, 7.32 ±0.09 Ma, and the Mesilau Porphyritic Granite, 7.22 ±0.07 Ma) deviate from the laccolith model having been emplaced laterally and around the periphery of the earlier units (Fig. 1c; Burton-Johnson *et al.,* 2017). Field evidence for the approximate volumes of the pluton's composite units (Fig. 1c, Burton-Johnson *et al.*, 2017) and the U-Pb zircon ages (Cottam *et al.*, 2010) give a total pluton volume of ~170 km^3 and a total emplacement period of 0.6 Ma. This equates to an average emplacement rate of ~3 $x10^{-4}$ km^3yr^{-1}; comparable with evidence from other plutons worldwide (de Saint Blanquat *et al.*, 2011; Menand *et al.*, 2015).

METHODOLOGY

Samples were analysed from each granitic unit, from the turbidite overburden of the Crocker Formation, and from a xenolith found in the intrusion (a conglomerate within the Donkey Granite, Fig. 1). Samples were powdered by fly press and agate ball mill.

Major element chemistry was obtained by XRF at Edinburgh University. Samples were dried at 1100°C, mixed with $LiBO_2$ flux and fused into glass discs for analysis (Gill, 1997). Trace element chemistry was obtained on a ThermoScientific X-Series 2 ICP-MS (Durham University). The methodology, blank, and detection limits are given in Ottley *et al.* (2003). Sample powders were dissolved using HF and HNO_3, and blanks, repeated samples and the standards BHVO-1, W2 and AGV-1 analysed for calibration and QC (Ottley *et al.,* 2003). To ensure zircon dissolution, granitic samples were fused prior to crushing and dissolution. Accuracy and reproducibility were monitored using standards AGV-1, BHVO-1, and W2, and through replicate

137 analysis of Mt Kinabalu samples (Supplementary Material 1 and Burton-Johnson,
138 2013).

139 Radiogenic isotope chemistry was obtained by Plasma Ionisation Multi-collector
140 Mass Spectrometer (PIMMS, Durham University). Sr and Nd isotopic analyses
141 followed the column chemistry procedures of Charlier *et al.* (2006). Whole rock
142 powders were dissolved in HF and HNO_3 SpA acid and separated by column
143 chemistry using Sr-spec resin and Hf-Nd cation resin (AG50 X-8). The lead fraction
144 was collected in 100µl 8N HCl from the Sr columns following collection of the Nd
145 and Sr fractions and elution of waste using 200µl 2.5N HCl. The Pb fraction was
146 dried down, dissolved in 500µl 3% HNO_3, and spiked with ^{206}Tl to correct for mass
147 bias (Hirata, 1996). PIMMS analytical procedures are detailed in Nowell *et al.*
148 (2003). For Nd and Sr, measured values for the NBS987 and J&M standards (±2SD
149 error) during the same run as the samples were 0.710269 ±23 (n=35) and 0.511110
150 ±11 (n=44) respectively. Data are corrected to the respective NBS987 and J&M
151 standard values of 0.71024 (Thirlwall, 1991) and 0.511110 (Royse *et al.,* 1998). For
152 Pb, measured values for the NBS981 standards ±2SD for $^{206}Pb/^{204}Pb$, $^{207}Pb/^{204}Pb$,
153 $^{208}Pb/^{204}Pb$, $^{207}Pb/^{206}Pb$ and $^{208}Pb/^{206}Pb$ (n=20) are 16.9405 ±9, 15.4981 ±9, 36.7177
154 ±23, 0.91486 ±3 and 2.1674 ±1 respectively. Data are corrected to the respective
155 values of NBS981 of 16.9405, 15.4980, 36.7174, 0.91485 and 2.1674 (Galer, 1997).

156 Oxygen isotope ratios of mineral separates were analysed by laser fluorination
157 (SUERC, East Kilbride). Oxygen was extracted by heating c. 1mg of sample with a
158 laser in the presence of ClF_3 (Mattey and Macpherson, 1993). Oxygen was converted
159 to CO_2 and isotopic ratios were analysed using a VG PRISM 3 dual inlet mass
160 spectrometer. Results are reported as $\delta^{18}O$ values in per mille (‰) deviations from
161 Vienna Standard Mean Ocean Water (V-SMOW). For precision, all sample analyses

were repeated. Four analyses of the reference standards SES, GP147 and UWG2 were made each day for daily calibration, and their mean daily standard error from published isotopic values is 0.15‰ and the maximum daily standard error was 0.26%.

Major element mineral chemistry was determined for polished thin sections using a JEOL JXA-8100 Superprobe electron microprobe (EMP) paired with an Oxford Instruments INCA energy-dispersive microanalytical system (EDS) at Birkbeck College. Analyses were performed using an accelerating voltage of 15 kV, a beam current of 10 nA, and a beam diameter of 1 μm. Calibration used standards of natural silicates, oxides, and Specpure metals, and a ZAF correction procedure was applied. XFe^{3+} (Fe^{3+}/Fe_{total}) for individual minerals was calculated from the charge balance and stoichiometry.

RESULTS

Data for all whole rock major and trace element geochemical analyses are presented in Table 1, whole rock isotope data and mineral separate oxygen isotope data in Table 2. Major element mineral chemistry is presented in Supplementary Material 2.

Major and trace elements

Mineralogically the individual units that comprise the Mt Kinabalu intrusion are largely granites (Burton-Johnson *et al.,* 2017). Geochemically the Alexandra Tonalite/Granodiorite and Low's Granite are diorites and later units are granodiorites and syenodiorites (Fig. 2a). Our analyses show a similar range in compositions to previous analyses by Vogt and Flower (1989), but coupling geochemical data with

mapping (Burton-Johnson *et al.,* 2017) and geochronological data (Cottam *et al.,* 2010) allows us to recognise a more refined structure of units (Fig. 2). All units are sub-alkalic and enriched in potassium, with the Alexandra Tonalite/Granodiorite and Low's Granite classified as high-K calc-alkaline and the later units as shoshonitic (Fig. 2b). While Alexandra Tonalite/Granodiorite is weakly peraluminous all subsequent units are metaluminous. Amphibole chemistry is calcic and dominantly magnesio-hornblende in classification (Fig. 3).

Trace element ratios show that Kinabalu rocks display uniform, relative depletion in Nb and Ta, and enrichment of K and Pb. Such signatures are similar to continental crust or arc magmatism. Chondrite normalised REE plots (Fig. 4) show elevated LREE/HREE and concave middle to heavy REE. Each unit displays a negative Eu anomaly.

Radiogenic Isotopes

The Alexandra Tonalite/Granodiorite ($^{87}Sr/^{86}Sr_i$ ~0.7076; $^{143}Nd/^{144}Nd_i$ ~0.51247 (εNd -3.19); $^{206}Pb/^{204}Pb_i$ ~18.754) is consistently displaced farther from mantle compositions than the younger intrusive units ($^{87}Sr/^{86}Sr_i$ ~0.7066, $^{143}Nd/^{144}Nd_i$ ~0.51251 (εNd -2.39) and $^{206}Pb/^{204}Pb_i$ ~18.724). Likewise, the Mt Kinabalu isotopes are displaced to more radiogenic Sr and Pb, and less radiogenic Nd than uncontaminated, mantle-derived basalts from Borneo and the adjacent South China Sea (Fig. 5a, Chen *et al.,* 2008; Wang *et al.,* 2008; Macpherson *et al.,* 2010; Cullen *et al.,* 2013). Isotopically, Kinabalu rocks (Fig. 5) are more similar to Mesozoic granites from the South China Sea (Yan and Shi, 2009; Yan *et al.,* 2010), the Capoas granite of Palawan (Encarnación and Mukasa, 1997; Burton-Johnson, 2013), and

the least radiogenic rocks from Vietnam, Hong Kong and Yunnan (Thuy *et al.,* 2004). Pb data for the region's magmatism, including Mt Kinabalu, diverges from the Northern Hemisphere Reference Line (NHRL) towards an enriched mantle (EMII) composition (Fig. 5b, Zindler and Hart, 1986), as noted by previous authors (Hoang *et al.,* 1996; Yan *et al.,* 2008).

Oxygen Isotopes

$\delta^{18}O$ values range between +9.4 and +10.3‰ for quartz, and between +6.6 and +8.2‰ for hornblende (Fig. 6). By analysing both hornblende and quartz, post-crystallisation alteration of the oxygen isotope composition can be assessed. Equilibration at magmatic temperatures produces lower and more restricted $\Delta^{18}O_{quartz\text{-}hornblende}$ isotope values (where $\Delta^{18}O^{18}O_{quartz\text{-}hornblende} = \delta^{18}O_{quartz} - \delta^{18}O_{hornblende}$) than lower temperature equilibration with altering fluids. Measured $\Delta_{quartz\text{-}hornblende}$ values are equivalent to temperatures of 650-1100°C (Fig. 6; Lackey *et al.,* 2008, and references therein). Within error (Fig. 6), this range is reasonable for mineral-mineral equilibrium in felsic magma containing hornblende, which, at 200 MPa vapour-saturated conditions, should be stable below 960°C (±10°C) to a solidus temperature 675° (±25°C, Naney, 1983).

Assuming that $\delta^{18}O$ values of all minerals represent magmatic conditions, we can estimate magmatic $\delta^{18}O$ values for all the other minerals by employing $\Delta_{mineral\text{-}hornblende}$ values (Lackey *et al.,* 2008, and references therein) for the temperatures determined by $\Delta_{quartz\text{-}hornblende}$ thermometry. A $\delta^{18}O$ for the bulk magma from which each sample crystallised can then be calculated through mass balance using: 1. the estimated magmatic $\delta^{18}O$ of each phase, and 2. the modal proportions of each phase in each

237 sample (as measured by point-counting, Burton-Johnson *et al.,* 2017). We used this
238 methodology for determining whole rock $\delta^{18}O$ in preference to bulk sample analysis
239 of $\delta^{18}O$ due to the slow diffusion rate of oxygen in hornblende (Farver and Giletti,
240 1985). This method thus allows an estimate of magmatic $\delta^{18}O$ without the influence
241 of meteoric water alteration, which would otherwise result in sub-solidus $\delta^{18}O$
242 alteration of phases possessing a faster diffusion rate (e.g. quartz and feldspar).

243

244 **DISCUSSION**

245
246 The only previous geochemical study of Mt Kinabalu (Vogt and Flower, 1989)
247 concluded that rocks of the Alexandra Tonalite/Granodiorite unit (then termed the
248 Biotite Quartz Monzodiorite by Vogt and Flower, 1989), represented the most
249 primitive magma in the intrusion and were produced by remelting of underplated
250 basalt. It was proposed that all other units (collectively referred to as Hornblende
251 Quartz Monzonite) were the result of further crustal contamination of the Biotite
252 Quartz Monzodiorite. Our isotopic data demonstrate that the Alexandra unit has the
253 most "crustal" isotopic ratios and so this relationship with the rest of the intrusion is
254 unlikely. Furthermore, the model developed by Vogt and Flower (1989) assumed
255 that the Alexandra unit was at the core of a nested diaper and so represented the
256 youngest unit of Kinabalu. Mapping and U-Pb geochronology of zircon has
257 subsequently demonstrated that the intrusion is layered with the Alexandra unit being
258 its oldest component (Fig. 1; Cottam et al., 2010).

259 Granitic melts can be derived through fractionation of mantle-derived melts, with or
260 without crustal assimilation (assimilation and fractional crystallisation, AFC), or
261 through partial melting of crustal lithologies (crustal anatexis) (e.g. Bogaerts *et al.,*

2006; Jagoutz *et al.*, 2009; Clemens and Benn, 2010; Chappell and White, 2011; Leuthold *et al.*, 2012; Jagoutz and Klein, 2018). We combine our new geochemical data with mapping and geochronological constraints to evaluate the likelihood that Mt Kinabalu magma was generated by these three mechanisms.

Crustal anatexis

Potential crustal sources for Mt Kinabalu magma are: (i) ophiolitic basement, (ii) turbidite sediments, (iii) older felsic continental crust beneath Sabah (previously postulated by Macpherson *et al.* 2010), (iv) continental crust under-thrust beneath Borneo during the final stages of Proto South China Sea subduction, or (v) gabbroic lower crust (Vogt and Flower, 1989). The isotopic ratios of Mt Kinabalu rocks are sufficiently displaced from mantle compositions for us to discount an origin solely from melting ophiolitic basement. However, the radiogenic isotopes cannot conclusively rule out the other possibilities, particularly as the turbidite sediments are variable in their composition, while the monzogranites and tonalites dredged from attenuated continental crust of the South China Sea share similar isotopic signatures to Mt Kinabalu (Fig. 5).

To evaluate the feasibility of producing Mt Kinabalu magma by crustal anatexis, we compiled data for melting experiments on igneous and sedimentary rocks and their metamorphic equivalents (Fig. 7). These experiments were conducted on a wide range of compositions over a range of temperatures, pressures, water contents and redox conditions. The alkali metal compositions show that the different protoliths produce melts with distinctive compositional ranges, regardless of the degree of melting (Fig. 7). Melting of a sedimentary protolith generates peraluminous melt compositions with

287 high K/Na and very low Ca/Na ratios, and with very restricted ratios of Al/(Na+ K) :
288 Al/(Ca + Na + K) (Fig. 7). Melting felsic crustal protoliths yield similar compositions
289 but tend to have even higher and more scattered K/Na (Fig. 7a). None of these
290 protoliths generates comparable melts to the largely metaluminous, high-Ca/Na and
291 high K/Na samples from Mt Kinabalu.

292 Partial melts of basaltic lithologies range from peraluminous to metaluminous (~90%
293 are peraluminous) and their Al/(Na+ K) : Al/(Ca + Na + K) ratios can resemble
294 Kinabalu rocks (Fig. 7b). However, their generally low K/Na ratios and consistently
295 low Ca/Na ratios (Fig. 7a) suggest that these are also unlikely sources for the
296 Kinabalu magmas. This corroborates our earlier inference made on the basis of
297 isotopic ratios. Only melts derived from exceptionally Ca-rich and Na- and K-
298 deficient basaltic amphibolites (Wolf and Wyllie, 1994) possess Ca/Na ratios as high
299 as Kinabalu (Fig. 7a), but these are strongly peraluminous with exceptionally high
300 Al/(Na + K) and K/Na much lower than the Mt Kinabalu granitoids. This also means
301 that any mixture of such high Ca/Na melt with high K/Na sources would remain
302 peraluminous, dissimilar to Mt Kinabalu. Consequently, melts derived solely from
303 crustal anatexis, be they from a single source or any likely mixtures (including the
304 mafic lower crust), cannot reproduce the major element composition of Mt Kinabalu,
305 or other metaluminous and intermediate to high Ca/Na and K/Na magmatism.

306 Prouteau *et al.* (2001) suggested that the Kinabalu intrusion is adakitic. We dispute
307 an origin for Mt Kinabalu magma through melting of subducted oceanic crust as the
308 major element compositions of partial melts from hydrous, basaltic amphibolites
309 (Winther and Newton, 1991; Sen and Dunn, 1994; Rapp and Watson, 1995) are
310 distinct from the Kinabalu rocks (Fig. 7). Neither our data nor that from preceding
311 studies (Vogt and Flower, 1989) possess the distinctive trace element signatures of

these putative slab melts (Defant and Drummond, 1990). Furthermore, the radiogenic isotope ratios of all Kinabalu units lie outside the fields of most ocean floor basalts, including the South China Sea (Fig. 4). Therefore, we dismiss this as a possible origin for the Kinabalu magmas.

Fractional crystallisation of mantle-derived basalt

Experimental petrology demonstrates the potential for fractional crystallisation of mafic magmas to produce granitic melts (e.g. Grove *et al.,* 2003; Alonso-Perez *et al.,* 2009; Nandedkar *et al.,* 2014; Müntener and Ulmer, 2018). There is no evidence in the immediate vicinity of Mt. Kinabalu for contemporaneous mafic magmatism, but Neogene basaltic volcanism occurred in other north Borneo locations, such as Semporna, Usun Apau and Linau Balui (Fig. 1a, Macpherson *et al.,* 2010; Cullen *et al.,* 2013), with evidence of differentiation to more felsic compositions of these locations. However, fractional crystallisation alone cannot be responsible for the range of Kinabalu magma compositions. The isotope ratios of Sr, Nd and Pb are all substantially displaced from those of Neogene basalt from Borneo, other than those identified as having experience substantial crustal contamination (Fig. 5; Macpherson et al., 2010). There is also significant variation between the different Kinabalu units, without large contrasts in trace element ratios, which are more readily reconciled with open-system behaviour in the crust. This is further suggested by the large range of oxygen isotope ratios, which include values for mafic phases, such as hornblende, that are substantially higher than those that would be expected to be in equilibrium with mantle-derived magma (Mattey *et al.,* 1994; Macpherson and Mattey, 1998; Lackey *et al.,* 2008). Therefore, we conclude that the isotopic diversity of the Mt Kinabalu

granitic intrusion cannot be explained by the fractionation of mantle-derived basalt alone, and instead requires open-system processes in the Borneo crust.

Crustal contamination of magma: Equilibrated Major Element – Assimilation with Fractional Crystallisation (EME-AFC)

To model open-system behaviour for the various geochemical properties considered here we developed an incremental major element AFC model of Equilibrated Major Element AFC (EME-AFC). This was undertaken because the thermodynamic model MELTS (Ghiorso and Sack, 1995) is not recommended for felsic or intermediate systems, and neither MELTS or rhyolite-MELTS (which can model high-silica systems, Gualda *et al.*, 2012) can model hydrous magmatic systems involving substantial hornblende or biotite fractionation. The Magma Chamber Simulator (Bohrson *et al.*, 2014) utilises MELTS, so is also unable to model systems involving significant fractionation of hydrous phases. Additionally, mass balance equations do not reflect the changing compositions of mineral phases in response to the geochemical evolution of the magma. Instead we developed EME-AFC modelling, which employs two-component major element partition coefficients ($K_D^{X,Y}=(X^{Min}.Y^{Liq})/(Y^{Min}.X^{Liq})$), where X and Y are elements in a single mineral phase (^{Min}) in equilibrium with a liquid (^{Liq}). This allows simultaneous modelling of major elements by EME-AFC, and trace elements, radiogenic isotopes, and oxygen isotopes by recognised methods (DePaolo, 1981).

The major element component of EME-AFC is similar to that of Grove and Donnelly-Nolan (1986) in which the Fe-Mg and Ca-Na compositions of the fractionating phases equilibrate with the evolving magma. This involved calculating the Fe-Mg and Ca-Na

phase compositions using two-component major element partition coefficients ($K_D^{Fe,Mg}=(Fe^{Min}.Mg^{Liq})/(Mg^{Min}.Fe^{Liq})$ and $K_D^{Ca,Na}=(Ca^{Min}.Na^{Liq})/(Na^{Min}.Ca^{Liq})$) and solving for successive increments of fractionation (*F*). We broadened this approach to a larger number of phases, equilibrating more elements and calculating the concentrations of all major and minor elements in each phase. Assimilation is modelled at each increment by binary mixing for the major elements according to a user-determined rate, *r* (the mass assimilated / mass crystallised), which is the parameter in AFC modelling describing the ability of magma to assimilate crust (DePaolo, 1981; Reiners *et al.,* 1995). The formulae for each phase and the sites into which elements can substitute are determined from Deer *et al.* (1992) and the valency of each element. The Fe-Mg, Al-Si and K-Na partition coefficients (Table 3) are determined from experimental data (Grove *et al.,* 2003; Alonso-Perez *et al.,* 2009; Nandedkar *et al.,* 2014). Note that, unlike trace element partition coefficients (Supplementary Material 6), two-component major element partition coefficients have narrow ranges of values (Table 3). Consequently, as in the "Crustal anatexis" section, our subsequent discussion of the EME-AFC modelling focuses on the major elements.

Plagioclase fractionates as $((K,Na)_{1-(x-1)},(Mg+Mn+Ca)_{x-1})_1((Fe+Al)_x,Si_{4-x})_4O_8$ and its equilibrium with the coexisting evolving liquid is determined by the two-component distribution coefficient $K_D^{Al,Si} = Al^{Plag}Si^{Liq}/Si^{Plag}Al^{Liq}$. The Al-Si distribution is used in preference to the Ca-Na distribution as $K_D^{Al,Si}$ in plagioclase is far less variable than $K_D^{Ca,Na}$ (1.8-4.2, compared to 0.6-16.2, Grove *et al.,* 2003; Alonso-Perez *et al.,* 2009; Nandedkar *et al.,* 2014). The Na-K distribution is calculated from $K_D^{K,Na} = K^{Plag}Na^{Liq}/Na^{Plag}K^{Liq}$. Fe substitutes for Al, and Mg, and Mn substitute for Ca in proportions determined empirically from the Mt Kinabalu mineral chemistry (Supplementary Material 3). Hornblende fractionates as $(Na,K)_{0-}$

$_1Ca_2((Mn,(Mg,Fe)),(Ti(Al,Si)))_{13}O_{22}(OH)$, and its equilibrium with silicate liquid is determined using the Fe-Mg and Al-Si two-component partition coefficients: $K_D^{Fe,Mg} = Fe^{Hb}Mg^{Liq}/Mg^{Hb}Fe^{Liq}$ and $K_D^{Al,Si} = Al^{Hb}Si^{Liq}/Si^{Hb}Al^{Liq}$. Orthopyroxene and clinopyroxene fractionate as $((Ca,Na),(Mn,(Mg,Fe)))_2(Si,(Ti,Al))_2O_6$ and use the Fe-Mg and Al-Si mineral-melt distribution coefficients: $K_D^{Fe,Mg} = Fe^{Opx}Mg^{Liq}/Mg^{Opx}Fe^{Liq}$, and $K_D^{Al,Si} = Al^{Cpx}Si^{Liq}/Si^{Cpx}Al^{Liq}$. Biotite fractionates as $(K,Na)_2((((Mg,Fe)Ti)Mn)_{4-6},(Al,Si)_{8-10})_{14}O_{20}(OH)_4$, and equilibrates with the liquid using $K_D^{Al,Si} = Al^{Plag}Si^{Liq}/Si^{Plag}Al^{Liq}$. Both olivine and garnet equilibrate using Fe-Mg mineral-melt partition coefficients and fractionate as $((Mg,Fe),Ca,Mn)_2(Si,Al,Ti)O_4$, and $(Mg,Fe)_3Al_2\ Si_3O_{12}$, respectively. Major and minor element concentrations not determined by two-component partition coefficients or stoichiometry are calculated for each phase by mean or linear regression correlations with other major elements in the mineral separate data (Supplementary Material 3). These calculations along with a detailed explanation of the major element modelling are presented in Supplementary Material 3 and Supplementary Material 4, as well as the EME-AFC modelling spreadsheet (Supplementary Material 5).

The trace element and isotopic components of EME-AFC are calculated at each increment using the AFC equations of DePaolo (1981). Trace element partition coefficients are compiled and calculated from the GERM database (https://earthref.org/KDD/) except quartz (Nash and Crecraft, 1985). Where reasonable, absent REE partition coefficients are interpolated. The compiled and calculated partition coefficients and their references are provided in Supplementary Material 6. Partial melting of the assimilant prior to assimilation in the melt is incorporated for the trace elements by batch modal melting with user-determined assimilant mineralogy and melt fraction ($F_{Assimilant}$).

To accommodate the changing nature of element partitioning during magmatic differentiation, EME-AFC employs four intervals of SiO_2 content representing melt compositions of basalt, basaltic andesite, andesite and rhyolite (note that the basaltic andesite starting material for the Mt Kinabalu models below is more evolved than the basaltic interval). Each interval uses appropriate major and trace element partition coefficients (Table 3). The two-component major element partition coefficients used in the EME-AFC model do not correlate with melt SiO_2 except for the Al-Si coefficient of plagioclase, which changes in the model at 57 and 63 wt.% SiO_2. In addition to the magmatic composition, at each increment the composition of the bulk cumulate assemblage, the total fraction of melt remaining in the system, and the total ratio of the mass of assimilated material to the initial magma mass (ρ) are calculated. To constrain the fit of the model through trial and error, the sum of the differences squared (ΣD^2) for the major elements of the model and target composition is also calculated.

Oxygen isotope fractionation between coexisting phases varies with temperature. Multivariate linear regression of experimental fractionation data for experimental conditions of 700-1300°C, 0-11% H_2O and 7-12 kbar, shows that melt SiO_2 contents correlate strongly with temperature (Fig. 8), moderately with H_2O but do not correlate with pressure (respective p-values of $6x10^{-13}$, 0.02 and 0.7). Thus, we derived an empirical relationship between SiO_2 and temperature ($T=-19SiO_2+2050$, R^2 = 0.75, ±62°C at 1SD). This allows the temperature, resultant $\Delta_{Mineral-Melt}$, $\delta^{18}O$ of the fractionating assemblage, and $\delta^{18}O$ of the magma to be calculated at each model increment.

Each potential fractionating phase has specific effects on the major element, trace element, and isotopic composition of the evolving melt. This means that, in

comparison with modelling geochemical properties in isolation, EME-AFC greatly limits the range of possible fractionating assemblages that can generate a target composition.

EME-AFC has specific advantages over existing AFC models: the ability to model felsic systems and those dominated by the fractionation of hydrous mineral phases (biotite and hornblende); simultaneous modelling of major and trace elements, and radiogenic and stable isotopes; control of the fractionating system and its parameters allows exploration of each parameter or input's effects on the liquid line of descent; and, importantly, the effects of pressure, water content and oxidation state of the system are accounted for by calibrating the model to the specific mineral chemistry of the system under consideration. In addition, the EME-AFC model is run within a standard spreadsheet, without the requirement for specialist software or specific operating systems.

Evaluation of EME-AFC modelling

EME-AFC modelling was developed to address the absence of AFC modelling solutions for felsic systems involving substantial amphibole or biotite fractionation. To validate this approach we compared the outputs of EME-AFC with those of Rhyolite-MELTS (Gualda *et al.*, 2012) for fractional crystallisation models of two discrete starting compositions: a Mid-Ocean Ridge Basalt (Allan *et al.*, 1989) and a basalt from Borneo (Macpherson *et al.*, 2010).

The detailed comparison (Supplementary Material 7) shows that EME-AFC broadly reproduces the liquid lines of descent (LLD) calculated by Rhyolite-MELTS (Fig. 9). For both starting compositions the largest discrepancy results from Rhyolite-MELTS fractionating high-Al clinopyroxene (>13.5 wt. % Al_2O_3) below 1075°C. Due to the relationship of Al and Si in the fractionating phase compositions (Table 3), this affects

461 Si as well as Al evolution. Consequently, remaining melt fractions are smaller in the
462 Rhyolite-MELTS models for the same SiO_2 concentration in EME-AFC. This also
463 influences the apparent LLD for all major elements compared with SiO_2. However,
464 neither suite shows evidence for the presence of high-Al pyroxene (Allan *et al.*,
465 1989). Pyroxenes in mafic lavas are expected to contain Al_2O_3 concentrations <9 wt.
466 %, and even lower concentrations are expected for metaluminous or MORB basalts
467 similar to those modelled (Le Bas, 1962; Nisbet and Pearce, 1977). Thus, the
468 suitability of the calculated Rhyolite-MELTS fractionating assemblage is ambiguous,
469 whilst the EME-AFC clinopyroxene Al_2O_3 compositions more similar to the expected
470 mineral chemistries of the settings modelled (Le Bas, 1962; Nisbet and Pearce,
471 1977).

472 **EME-AFC modelling of Mt Kinabalu**

473 A Linau Balui basaltic andesite sample (LB85, Cullen *et al.,* 2013) was chosen as the
474 initial melt. This is the most local basalt for which a comprehensive major element,
475 trace element, and radiogenic isotope dataset was available. The $\delta^{18}O$ value of LB85
476 is not known but the primary melts can be assumed to have a value of +5.5‰ due to
477 the limited variation magma derived from the mantle (5.5 ±0.35‰, Mattey *et al.,*
478 1994; Macpherson and Mattey, 1998). Metasedimentary xenoliths are the only
479 recorded field evidence for crustal assimilation at Mt Kinabalu (Vogt and Flower,
480 1989; Burton-Johnson, 2013). Thus a constant elemental and isotopic composition
481 from a metamorphosed conglomerate xenolith found within the Donkey Granite (Fig.
482 5) was used as the assimilant in the initial models.

483 Applying the model to the most voluminous unit of Mt Kinabalu, the King Granite,
484 most of the mineral chemistries (Fig. 10) and chemical variation of the pluton can be
485 generated through EME-AFC modelling with the exceptions of K and Na. Regardless

of the fractionating assemblage and degree of assimilation, the high-K chemistry of Mt Kinabalu cannot be replicated by assimilation of the meta-conglomerate xenolith (Fig. 11, Model 1). Experimental petrology has shown that partial melts of metasediments develop higher K than their protoliths (Fig. 7, Le Breton and Thompson, 1988; Vielzeuf and Holloway, 1988; Douce and Johnston, 1991; Gardien *et al.*, 1995; Montel and Vielzeuf, 1997). From these studies, the biotite, plagioclase, and quartz (BPQ) starting material for the melting experiments of Gardien *et al.* (1995) most closely resembles the mineralogy and chemistry of the meta-conglomerate. Incorporating this melt composition in to the EME-AFC model replicates the sense of K-enrichment required for the Alexandra unit (Fig. 11a, Model 2). However, the higher K-enrichment of the majority of units at Mt Kinabalu cannot be reproduced by this assimilant chemistry (Fig. 11a, Model 2) and the Na compositions of the Mt Kinabalu intrusive rocks are poorly reproduced (Fig. 11b, Model 2).

Increasing the modelled K_2O concentration of the BPQ assimilant further shows that the K_2O composition of Mt Kinabalu requires the assimilant to contain up to 12 weight % K_2O. Despite the range of protolith compositions, degrees of melting, and melt conditions of the compiled data for melting experiments (as used in Fig. 7), the highest K_2O concentration in the partial melt was 7.7 weight % from a metapelite (Douce and Johnston, 1991). Consequently, it is unlikely that the K-enrichment of Mt Kinabalu results from assimilation alone.

Instead, the simplest resolution to the offset from observed alkali contents is to postulate a wider range of precursor K-contents in the initial melts. A potential, contemporaneous analogue for such heterogeneity can be found in central Borneo. At 8 Ma, coincident the formation of the Mt Kinabalu intrusion, minette dykes were

511 emplaced at Linhaisai (Fig. 1a) as a result of low degree melting of a metasomatised,
512 fertile mantle source (Bergman et al., 1988). These possess K_2O contents ranging
513 from 2.15 to 6.30 wt.% in relatively low silica melts (Fig. 11a). These same minettes
514 also possess relatively low Na contents compared to Neogene basalts from Borneo
515 (Fig. 11b). It is unlikely that the volume of magma, or the heat to generate substantial
516 crustal melting at Kinabalu could be produced from a phase of minette-style
517 magmatism. However, the occurrence of contemporaneous high-K, low-Na
518 magmatism suggests that the mantle beneath Borneo may contain substantial
519 enrichment that could generate mafic precursors of a composition between that of
520 minette and the mafic, intraplate magma inferred for Semporna and Linau Balui
521 (Macpherson et al., 2010; Cullen et al., 2013). Increasing the primary magma K_2O to
522 2.5 wt. % and reducing the primary magmatic Na_2O from to 2.1 wt. % generates
523 metaluminous melts with alkali metal compositions similar to Mt Kinabalu (Fig. 11b
524 and 11c, Model 3).

525 The range of the King Granite compositions (including major and trace elements, and
526 isotopes) can be modelled by contamination of the modified primary melt (2.1 %
527 Na_2O, 2.5% K_2O) by a partial melt of the meta-conglomerate. In the absence of partial
528 melt data for the meta-conglomerate xenolith, this was simulated using the major
529 element composition of the BPQ partial melt used in Model 2 (Fig. 11, Gardien *et al.*,
530 1995) and the analysed trace elements of the xenolith, modelled to the same degree of
531 partial melting as the BPQ melting experiment ($F_{\text{Assimilant}} = 0.09$).

532 The King Granite compositions are generated through the bulk cumulate fractionation
533 of: 42-47% plagioclase, 14-17% clinopyroxene, 14-17% orthopyroxene, 18-20%
534 hornblende, 0.5% apatite, 1.5% magnetite, 3.5% ilmenite, and 0.01% zircon (Fig. 12;
535 Table 4). A $\delta^{18}O$ value of +10‰ is required for the assimilant, which is suitable value

for this siliclastic sedimentary lithology (Magaritz *et al.,* 1978). The degree of fractionation, *F* (the fraction of melt remaining) is 0.54-0.66, while the required assimilation rate, *r* (mass assimilated / the mass crystallised at each increment of *F*) is 0.4-0.57, resulting in a value for ρ (the total ratio of the mass of assimilated material to the initial magma mass) of 0.23-0.25.

Although energy constrained AFC modelling (EC-AFC, Spera and Bohrson 2001) is unable to model major elements, it can be used to determine thermodynamic constraints for our model. EC-AFC thus indicates that *r* values of 0.4-0.8 are reasonable for our system given the proposed input chemistries, pre-emplacement assimilation at mid-crustal depths, and temperatures of basaltic magma. Thermodynamic modelling of AFC processes has shown that *r* is variable during magmatic evolution (Reiners *et al.*, 1995) and, thus, the EME-AFC model (Supplementary Material 5) can accommodate variable *r*. However, in the interest of not overcomplicating the Mt Kinabalu models and presenting the EME-AFC methodology here for the first time, *r* is treated as a constant in this scenario.

Modelling the chemistries of the remaining units indicates that similar conditions could produce the other units. However, slight differences in chemistry indicate the broad evolution of the intrusion through its emplacement. The compositional range of the Donkey Granite, Paka Porphyritic Granite and Mesilau Porphyritic Granite are similar to the King Granite (Fig. 12) so can be replicated by similar EME-AFC parameters but with variations in the degree of fractionation (F = 0.5-0.74), r (0.36-0.66), and ρ (0.2-0.25). This is more marked for the less evolved compositional range of the earlier Low's Granite, which reflects significantly lower degrees of fractionation (F = 0.72-0.78). Despite this, isotopic ratios of the Low's Granite are similar to those of the more evolved units, suggesting a higher assimilation rate (r =

561 0.65-0.73, ρ =0.16-0.21). Likewise, a similar fractionating assemblage can also
562 produce the compositional range of the earliest unit, the Alexandra
563 Tonalite/Granodiorite (F = 0.59-0.73), but also requires a high rate of assimilation (r
564 = 0.56-0.72, ρ =0.22-0.29) and either no K-enrichment of the primary magma or more
565 complete melting of the assimilant (Fig. 10a). Alexandra also requires a higher
566 $^{207}Pb/^{204}Pb$ ratio in the assimilant than other units (Fig. 12), indicating isotopic
567 heterogeneity in the assimilant. The assimilation rate, r, in these two oldest units is
568 higher than those that follow but within the range of values predicted by EC-AFC.
569 The subsequent decrease in r may reflect the reduced fertility of the assimilant
570 following early intrusive episodes. As the source, assimilant, and fractionating
571 assemblages are similar for all units, this reduction in assimilation rate and the degree
572 of fractionation may have been the primary cause of geochemical heterogeneity in the
573 Mt Kinabalu intrusion.

574 Due to the pluton's exceptional vertical exposure, the contacts and composite unit
575 volumes can be constrained (Fig. 1, Burton-Johnson *et al.,* 2017). Combining this
576 with the outputs from the EME-AFC model allows us to estimate the volume of
577 mantle-derived magma emplaced into the crust and the volume of crust assimilated.
578 The total pluton volume (V_p) can be expressed as:

579 $$V_p = V_0 - V_c + V_a$$

580 [Eq. 1]

581 Where V_0 is the primary magma volume, V_c is the volume of fractionated material and
582 V_a is the volume of assimilated material. If V_c = (1-F) and $\rho = V_a/V_c$ then:

583 $$V_0 = (V_p + 1 - F)/(\rho + 1)$$

584 [Eq. 2]

585 Allowing a conservative 20% error in the volume estimation of the composite units,
586 the 140-210 km^3 total pluton volume can be generated by 115-176 km^3 of primary
587 magma and 25-43 km^3 of assimilated crust.

588

589 **Nature of the crustal contaminant**

590
591 As shown by EME-AFC modelling, partial melts of the conglomerate xenolith are a
592 suitable analogue for the crustal contaminant required to generate the chemical
593 heterogeneity of intrusive units at Mt Kinabalu. Further insight into the nature of the
594 contaminating crust can be gained by comparing the inherited zircon population of Mt
595 Kinabalu (Cottam *et al.,* 2010) to the detrital zircon populations of the regional
596 sedimentary units (Fig. 13. van Hattum *et al.,* 2013). The Mt Kinabalu zircon
597 population has a prominent inherited population with ages of 96 to 147 Ma, with rare,
598 older Mesozoic ages and very few Palaeozoic or Precambrian Ages (Fig. 13). This
599 contrasts with zircon populations hosted in the region's deep-water turbidite deposits
600 of the Oligocene units of the Crocker Formation and the Eocene Sapulut and
601 Trusmadi Formations, which each have a substantial population of early Mesozoic
602 and Palaeozoic zircons, with or without notable Precambrian peaks (Fig. 13). The
603 Upper Eocene unit of the Crocker Formation displays a very similar distribution of
604 inherited zircon age to Mt Kinabalu (Fig. 13) and, therefore, represents the most likely
605 local, siliclastic source of the xenolith and the contaminant of the magma that
606 constructed the pluton.

607

608 **Origin of the magmatism**

609

610 Mt Kinabalu is isolated from any contemporaneous mafic or felsic magmatism.
611 Intraplate basalts and andesites from the Semporna peninsula (Fig. 1a) are the closest
612 occurrence of magmatism but are younger than Kinabalu and appear to have been
613 generated under lithosphere that was previously thinned by subduction between the
614 Celebes and Sulu seas (Macpherson *et al.,* 2010). The Semporna magmatism may
615 also be associated with other younger sites in central, northern Borneo, such as Usun
616 Apau and Linau Balui (Cullen *et al.,* 2013), and possibly as far afield as Niut in
617 western Borneo (Harahap, 1994); but the difference in ages of these events suggests
618 there is no direct link with Mt. Kinabalu.

619 The only contemporaneous magmatism on the island is the Linhaisai minette in
620 central Borneo (Fig. 1a) for which K-Ar dating of phlogopite (7.8 ±0.3 Ma, Bergman
621 *et al.*, 1988) gives almost identical ages to U-Pb dating of Kinabalu zircon (7.22-7.85
622 Ma, Cottam *et al.*, 2010). As discussed above, the large distance between these
623 suggest it is unlikely that they are part of the same magmatic system. However, the
624 emplacement of two magmatic bodies, each requiring an input of primitive magma
625 from an enriched mantle source, suggests that regional controls on mantle melting
626 may have operated at this time.

627 Structural and Anisotropic Magnetic Susceptibility data (Burton-Johnson *et al.,*
628 2019) indicate that Mt Kinabalu was emplaced into a zone of NNW-SSE extension,
629 possibly the result of SE-directed slab rollback during Celebes Sea subduction to
630 the SE (Cottam *et al.,* 2013; Hall, 2013). Extension of the crust may have provided
631 pathways through which relatively low-degree partial melts from enriched mantle
632 could intrude and heat the crust, allowing generation of a body composed of both
633 mantle and crustal melts. If extension was sufficient then lithospheric thinning may
634 have resulted in further mantle upwelling, enhancing the degree of melting and the

volume of melt produced at Mt Kinabalu. The Linhaisai minette was emplaced as a series of dykes with a broad northerly trend (Bergman *et al.,* 1988), suggesting there was also extension in central Borneo at this time. The Linhaisai minette dykes represent a more restricted event with a lower degree of partial melting, which is suggested not only by its restricted, preserved volume but also by its silica-undersaturated composition. Such magmatism would transport limited heat into the crust, which is consistent with the lack of evidence for crustal contamination here (Bergman *et al.,* 1988). Taken together, the two localities are consistent with an origin as intraplate, mafic magmatism. The major distinction is that at Mt Kinabalu there was a sufficient flux of magma, and heat, to promote melting of, and contamination by, the local upper crust.

Distribution of the EME-AFC Model

For application to other studies, a user-friendly spreadsheet of the EME-AFC model used in this study is available with instructions for download and utilisation in Supplementary Material 5 (both a blank template spreadsheet, 5a, and an example spreadsheet completed for Mt Kinabalu, 5b. Alternatively, access [URL/DOI of spreadsheet to be finalised post-acceptance] or contact the lead author for the latest version.

CONCLUSIONS

- The primary magma of Mt Kinabalu was a partial melt of fertile, metasomatised, high-K, low-Na mantle. This may have been similar to the source for the contemporaneous Linhaisai minette magmatism in central

660 Borneo, which would have resulted from lower degrees of melting.
661 Magmatism was contemporaneous with and driven by regional crustal
662 extension, possibly linked to a slab rollback during subduction of the Celebes
663 Sea to the SE.

664 - Compiled experimental data shows that metaluminous melts with both Ca/Na
665 > 1.5 and K/Na > 0.5 (Fig. 7), including Mt Kinabalu, cannot be generated
666 through crustal anatexis.

667 - Fractional crystallisation of plagioclase, pyroxene, and amphibole rich
668 cumulates from initial Mt Kinabalu magmas was accompanied by assimilation
669 of partial melts of siliclastic sediments; most probably the basal units of the
670 Crocker Formation. Combined with metasomatism of the mantle source, this
671 imparted a high-K to shoshonitic chemistry to the granitoids. The fertility of
672 the contaminating crust reduced after emplacement of the initial two granitic
673 units, reducing the assimilation rate in subsequent magmatism. This variation
674 in assimilation rate produced the geochemical heterogeneity of Mt Kinabalu.

675 - Evidence for the derivation of Mt Kinabalu granitic magmatism from
676 assimilation and fractional crystallisation was determined through a new
677 approach to AFC modelling of major and trace elements, and radiogenic and
678 stable isotope ratios. The major and minor element chemistry of each
679 fractionating phase is calculated to be in magmatic equilibrium using
680 experimentally derived two-component partition coefficients at each stage of
681 this incremental model (Equilibrated Major Element Assimilation and
682 Fractional Crystallisation modelling, EME-AFC).

683

ACKNOWLEDGEMENTS

We thank Wendy Bohrson, Frank Spera, Hervé Rezeau, and an anonymous reviewer for their thorough reviews of this paper, and Wendy Bohrson and Marjorie Wilson for their work as editors. We are additionally indebted to Wendy Bohrson for her discussions during revision of the manuscript. NERC supported this study through a PhD studentship to AB-J and access to the Isotope Community Support Facility at SUERC. We wish to thank Alim Biun, Felix Tongkul and Maklarin Lakim for their assistance in facilitating the field season; Jamili Nais of Sabah Parks who allowed us to work in the National Park; the mountain guides and researchers of Mt Kinabalu National Park, especially Alijen "Jen", Halli, Jasirin, Sokaibin, Maklarin Lakim, Sapinus, Samuel and Nicholas; and we thank Robert Hall, Mike Cottam and the SE Asia Research Group at Royal Holloway for their support throughout this project.

REFERENCES

Automatic citation updates are disabled. To see the bibliography, click Refresh in the Zotero tab.

Figure and Table Captions

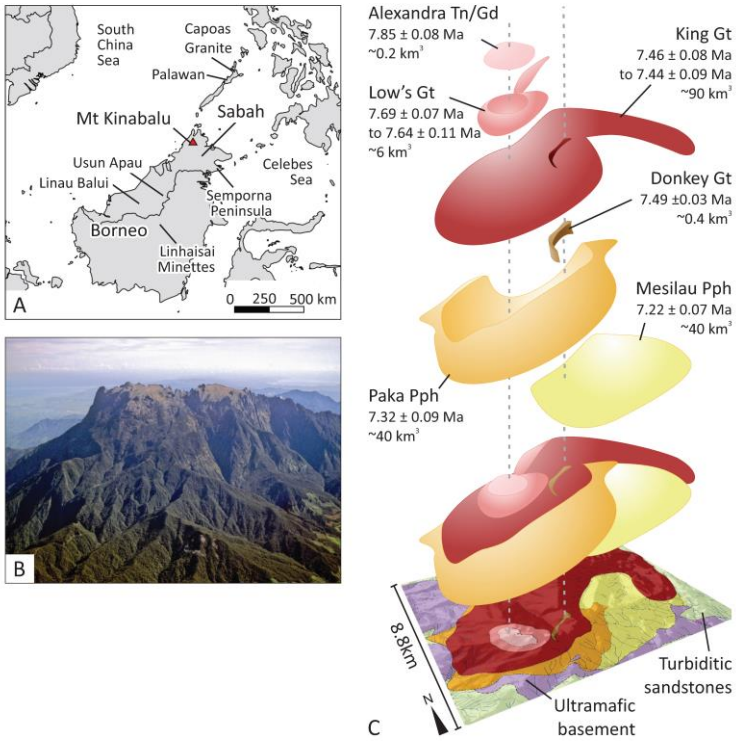

Fig. 1. A) Regional geography of Mt Kinabalu and the locations referred to in the text within SE Asia. B) Aerial photograph of Mt Kinabalu from the south highlighting its extreme vertical relief; courtesy of Tony Barber. C) Internal structure and U-Pb zircon emplacement ages of the Mt Kinabalu intrusion (Cottam *et al.,* 2010; Burton-Johnson *et al.,* 2017). Volumes were determined using field relations and contact orientations, as discussed in Burton-Johnson *et al.* (2017). Abbreviations: Tn – Tonalite, Gd – Granodiorite, Gt – Granite, Pph – Porphyritic Granite.

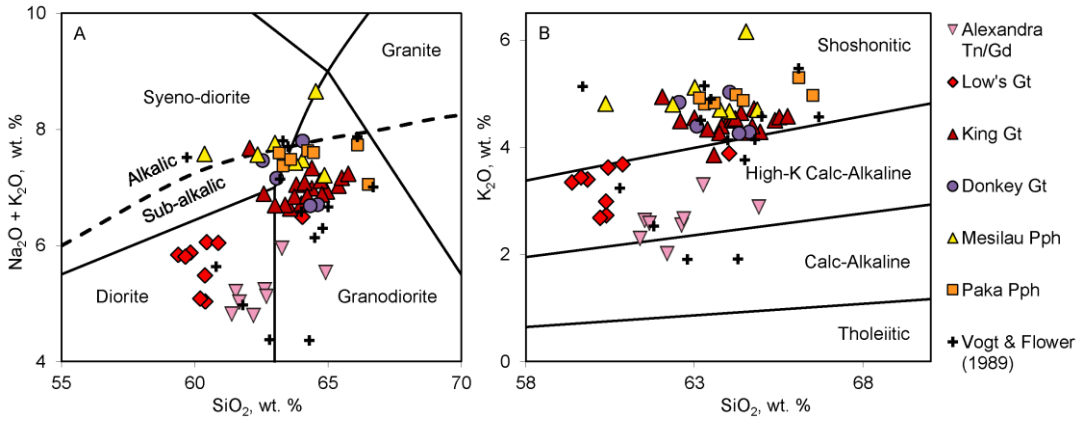

713

714 Fig. 2. Geochemical classification diagrams of the Mt Kinabalu granitoids. A) TAS
715 diagram of Cox *et al.* (1979). B) K_2O vs silica diagram of Le Maitre *et al.* (1989).
716 Abbreviations as in Fig. 1. Existing data shown for comparison (Vogt and Flower,
717 1989).

718

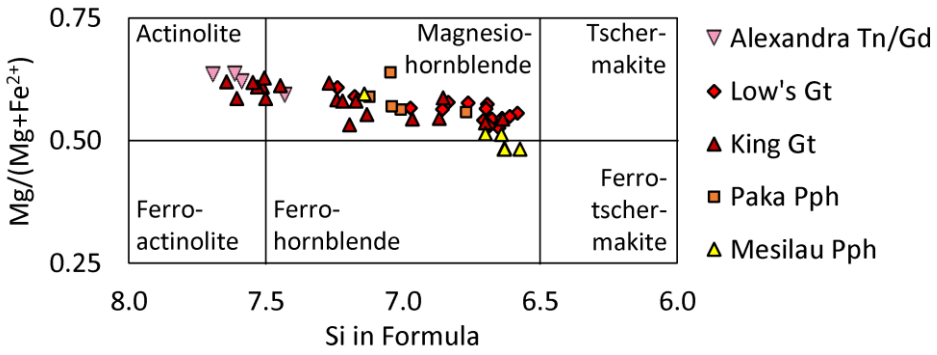

719

720 Fig. 3. Amphibole chemistries, following the Leake *et al.* (1997) classification for
721 calcic amphiboles.

722

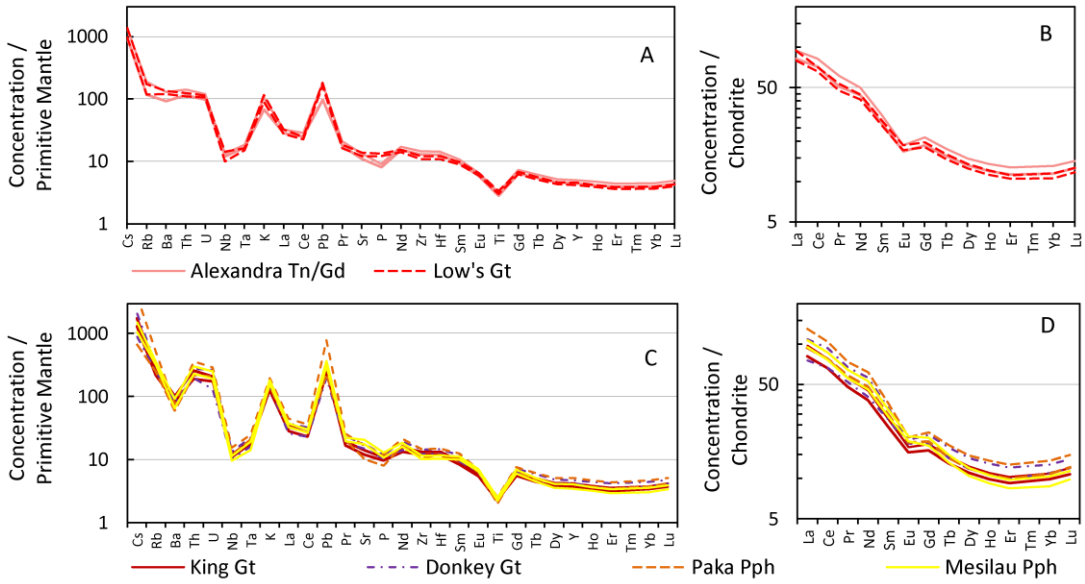

723

724 Fig. 4. Multi-element, primitive mantle normalised trace element plots and chondrite
725 normalised REE plots for the Mt Kinabalu granitic units. Plots show the upper and
726 lower 95% confidence limits for each unit. Normalising values from Sun and
727 McDonough (1989). Abbreviations as in Fig. 1.

728

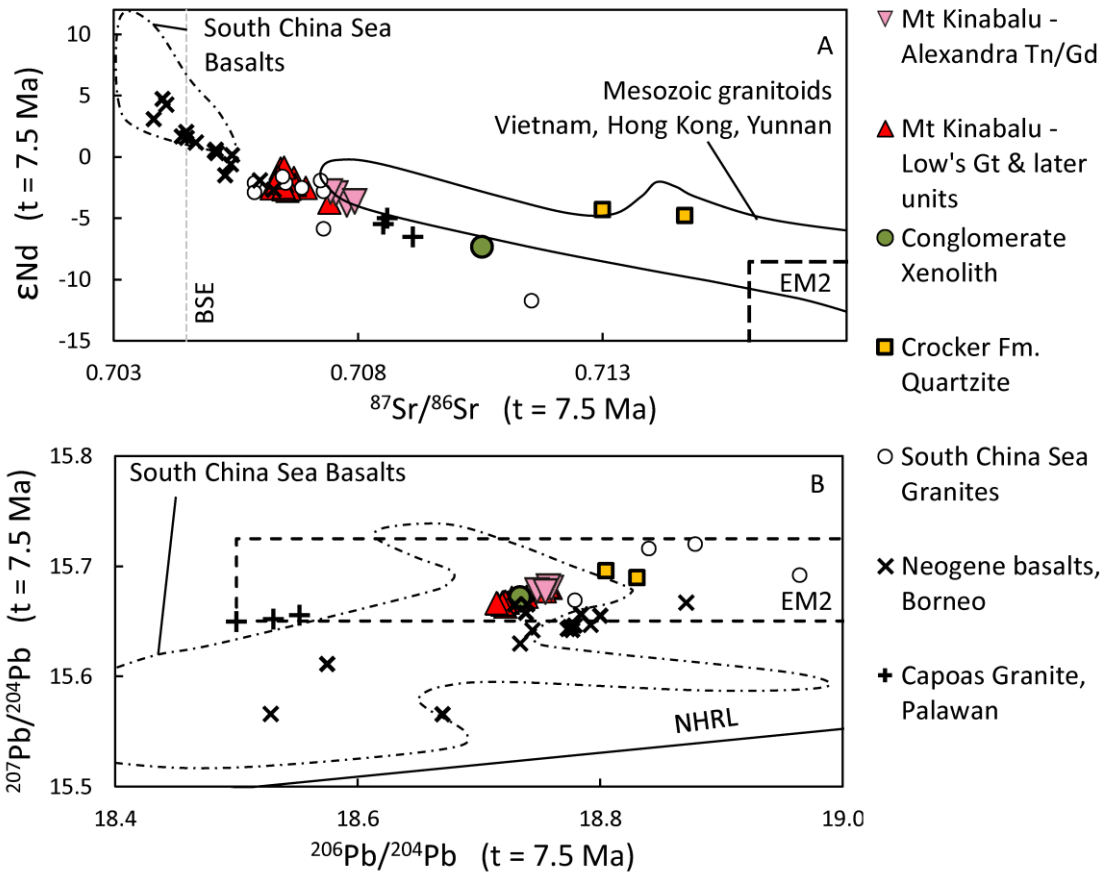

729

730 Fig. 5. Sr, Nd and Pb isotope ratios Mt Kinabalu granitic rocks at 7.5Ma. Data for
731 comparison: South China Sea basalts (Tu *et al.,* 1992; Yan *et al.,* 2008); Mesozoic
732 granites of the South China Block and Yangtze Block (Zhu, 1995); Mesozoic
733 Granitoids of Vietnam (Thuy *et al.,* 2004), Hong Kong (Darbyshire and Sewell,
734 1997) and Yunnan Province (Yanbo and Jingwen, 2010); Neogene basalts from
735 Borneo (Macpherson *et al.,* 2010; Cullen *et al.,* 2013); Mesozoic granites from the
736 South China Sea (Yan *et al.,* 2010, 2011); Spreading centre basalts of the Indian
737 Ocean from the PetDB database (http://www.earthchem.org/petdb); Northern
738 Hemisphere Reference line (NHRL) backdated to 7.5Ma using the mean U & Pb
739 concentrations of the I-MORB data (Hart, 1984). EM2 fields from Zindler and Hart
740 (1986). Bulk Silicate Earth (BSE) from Faure (1986). Abbreviations as in Fig. 1.

741

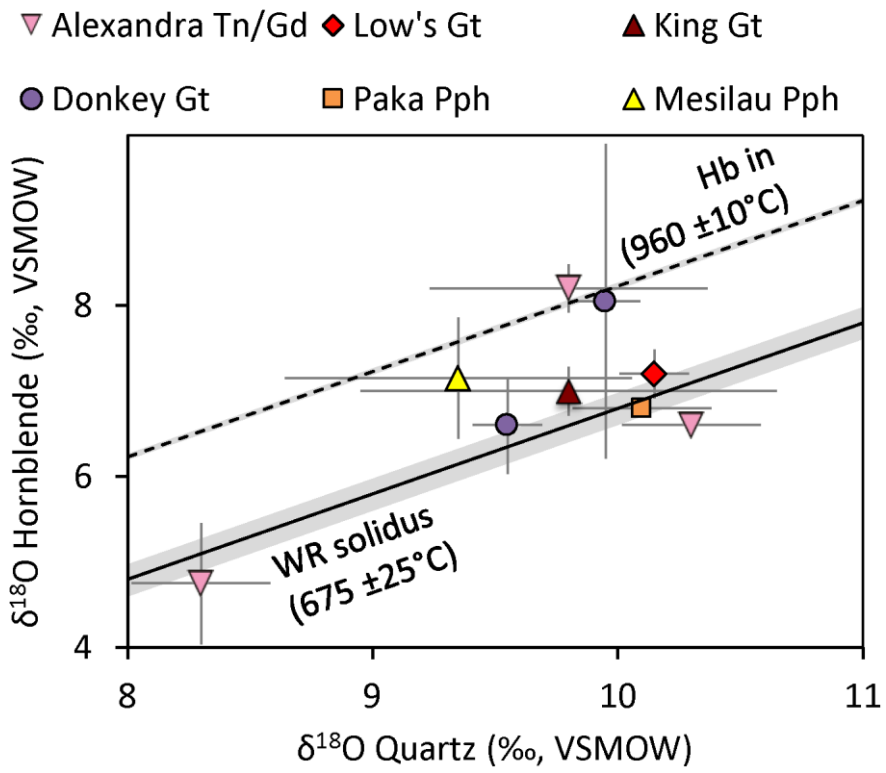

742

743 Fig. 6. $\delta^{18}O$ values of quartz and hornblende in Mt Kinabalu rocks. 2SD error bars
744 based on replicate analyses of each mineral from the same sample. Calculated
745 isotherms and associated errors (grey shaded regions) shown for the whole rock
746 solidus and hornblende crystallisation temperatures for the vapour saturated 200MPa
747 experiments of Naney (1983) (calculated from Clayton *et al.*, 1989; Kohn and
748 Valley, 1998; Chacko *et al.*, 2001; Valley, 2003; Lackey *et al.*, 2008). Abbreviations
749 as in Fig. 1.

750

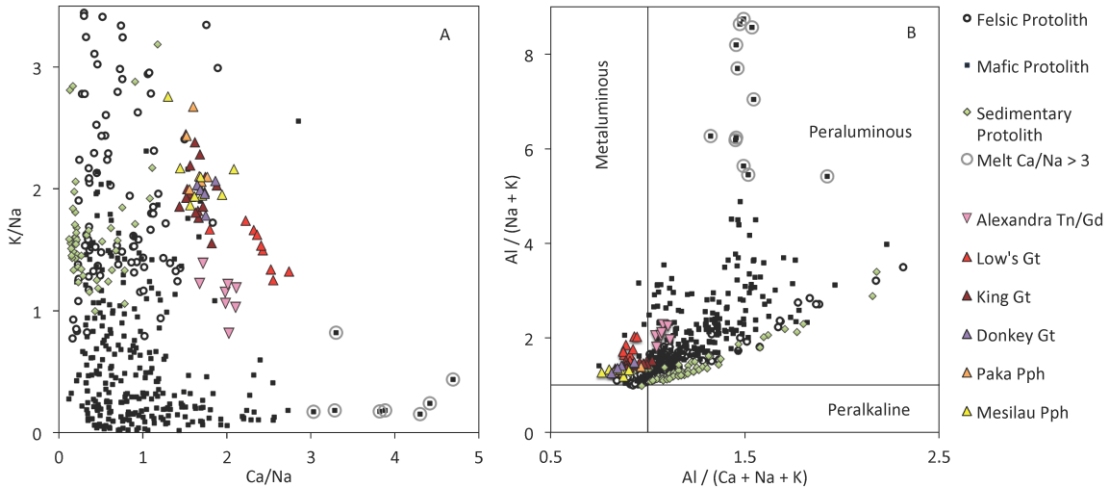

751

752 Fig. 7. Comparison of the Mt Kinabalu data with collated melting experiment data for
753 melting experiments on potential felsic sources (tonalites and felsic gneisses), mafic
754 sources (basalts and basaltic amphibolites), and sedimentary sources (sediments and
755 metasediments) (Vielzeuf and Holloway, 1988; Beard and Lofgren, 1991; Douce
756 and Johnston, 1991; Rapp *et al.*, 1991; Rushmer, 1991, 1993; Winther and
757 Newton, 1991; Skjerlie and Johnston, 1992; Sen and Dunn, 1994; Wolf and
758 Wyllie, 1994; Douce and Beard, 1995; Gardien *et al.*, 1995, 2000; Rapp and
759 Watson, 1995; Singh and Johannes, 1996a, 1996b; Winther, 1996; Montel and
760 Vielzeuf, 1997; Patino Douce, 2004; Sisson *et al.*, 2005; Xiong *et al.*, 2005; Xiao
761 and Clemens, 2007). Note that the samples from mafic sources showing Ca/Na
762 values >3 (highlighted in circles) are peraluminous with high Al/(Na+K) values.
763 Crustal values from Rudnick and Gao (2003). Abbreviations as in Fig. 1.

764

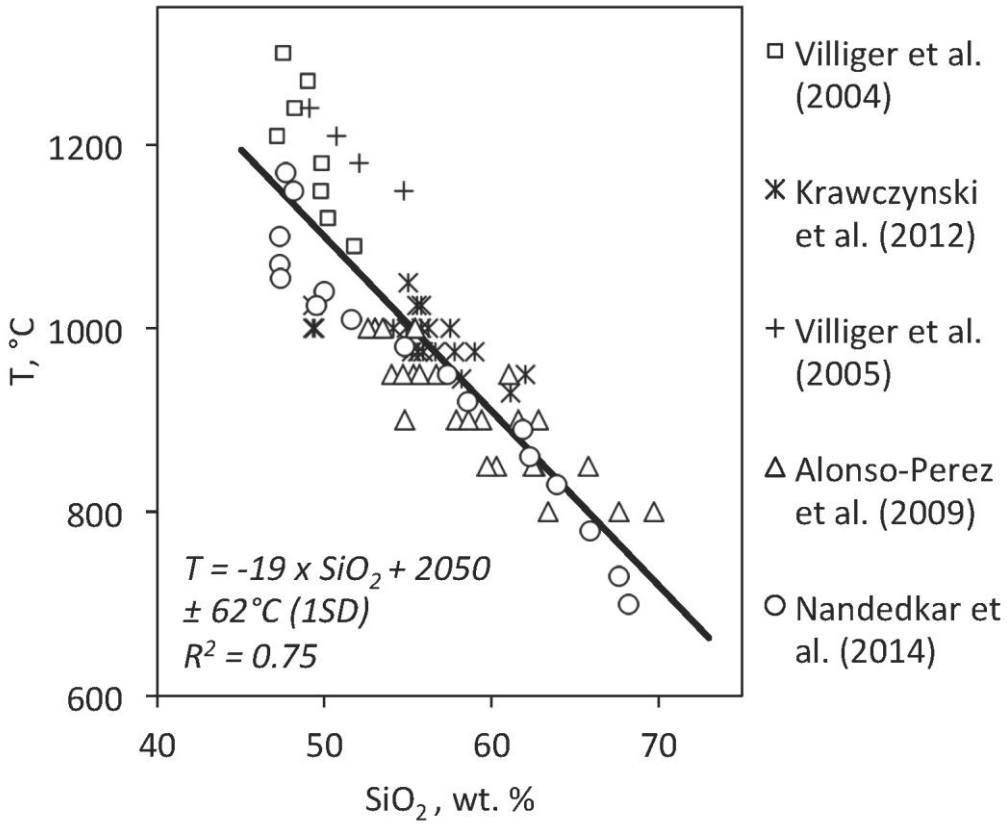

765

766 Fig. 8. Temperature vs SiO_2 for glasses from published crystallisation experiments
767 and empirical relationship derived by linear regression (Villiger *et al.*, 2004; Villiger,
768 2005; Alonso-Perez *et al.*, 2009: 200; Krawczynski *et al.*, 2012; Nandedkar *et al.*,
769 2014).

770

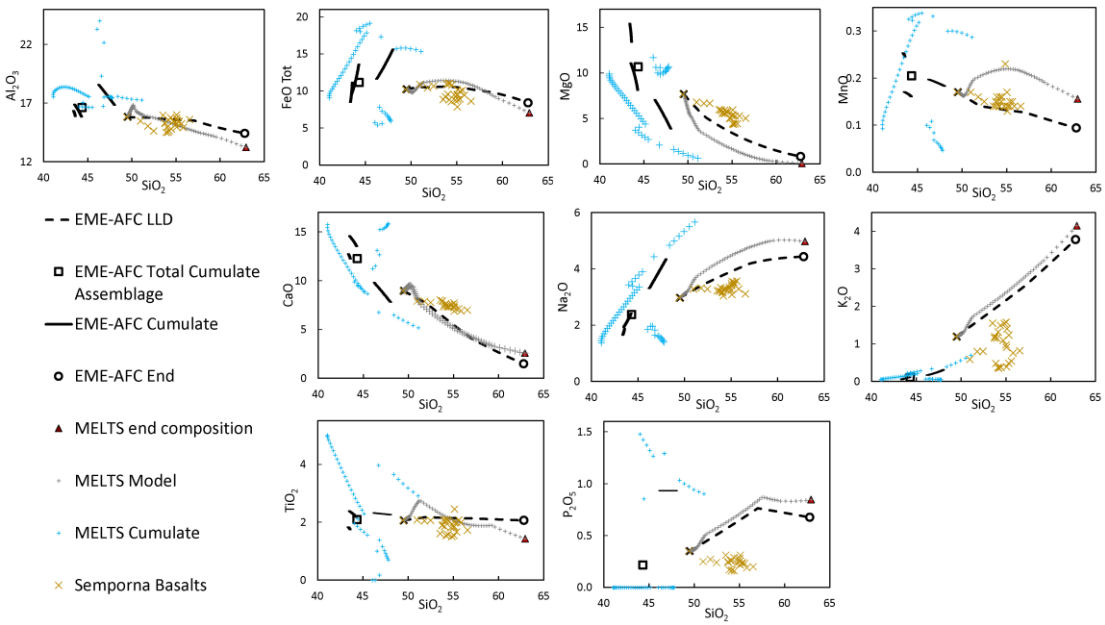

771

772 Fig. 9. Liquid lines of descent (LLD) of major elements (wt. %) for basalt SBK13
773 from Semporna, northeast Borneo (Macpherson *et al.*, 2010), compared with
774 fractionating assemblages from Rhyolite-MELTS and EME-AFC models. Whole rock
775 (WR) compositions of the basaltic suite are shown for comparison (Macpherson *et al.*,
776 2010). Note that these are fractional crystallisation only models, and the discrepancy
777 between the models and sample data in the Na_2O and K_2O plots highlights the effect
778 of crustal assimilation on the differentiation of the Bornean basaltic suite
779 (Macpherson *et al.*, 2010).

780

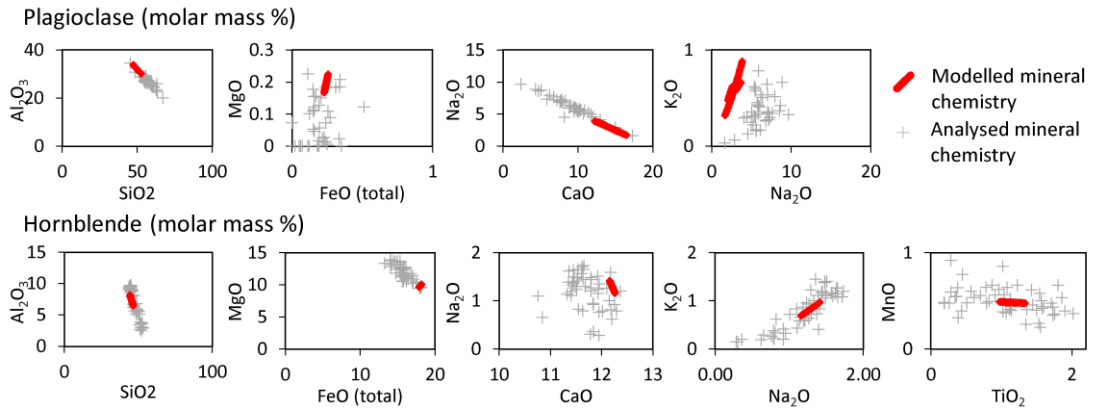

781

782 Fig. 10. Molar mass % of the analysed mineral chemistries of Mt Kinabalu and EME-

783 AFC modelled mineral chemistries of the King Granite.

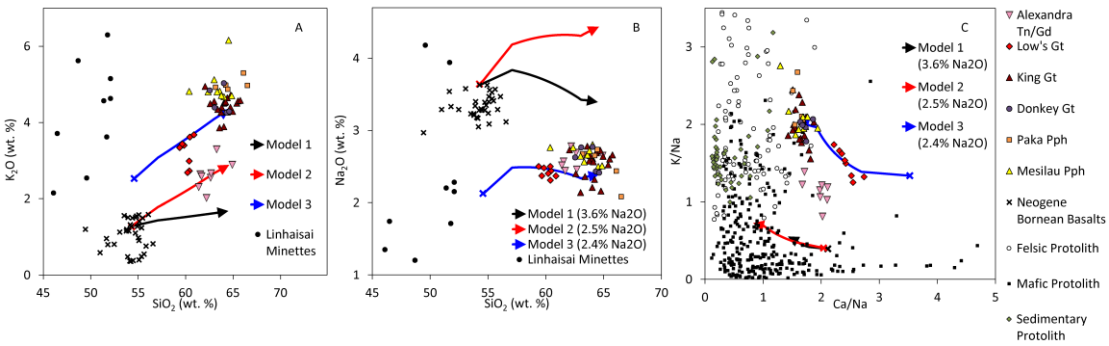

784

785 Fig. 11. Alkali metal chemistries of Mt Kinabalu granites and models to simulate

786 assimilation with fractional crystallisation. (a) K_2O versus SiO_2, (b) Na_2O versus

787 SiO_2, (c) K/Na versus Ca/Na. Model 1 (black): Linau Balui basalt (LB85; Cullen et

788 al., 2013) contaminated by the bulk chemistry of meta-conglomerate xenolith from

789 the Donkey Granite. Model 2 (red): LB85 contaminated by partial melt of biotite,

790 plagioclase and quartz-bearing starting material (BPQ) of Gardien *et al.* (1995):

791 Model 3 (blue) Starting material with modified alkali contents as discussed in text

792 contaminated by BPQ partial melt (as in Model 2). Experimental melt data in (c) as in

793 Fig. 7. Neogene basalt data from Macpherson *et al.* (2010) and Cullen *et al.* (2013).

794 Note that Model 1 is larger overlain by Model 2 in (c). Abbreviations as in Fig. 1.

795

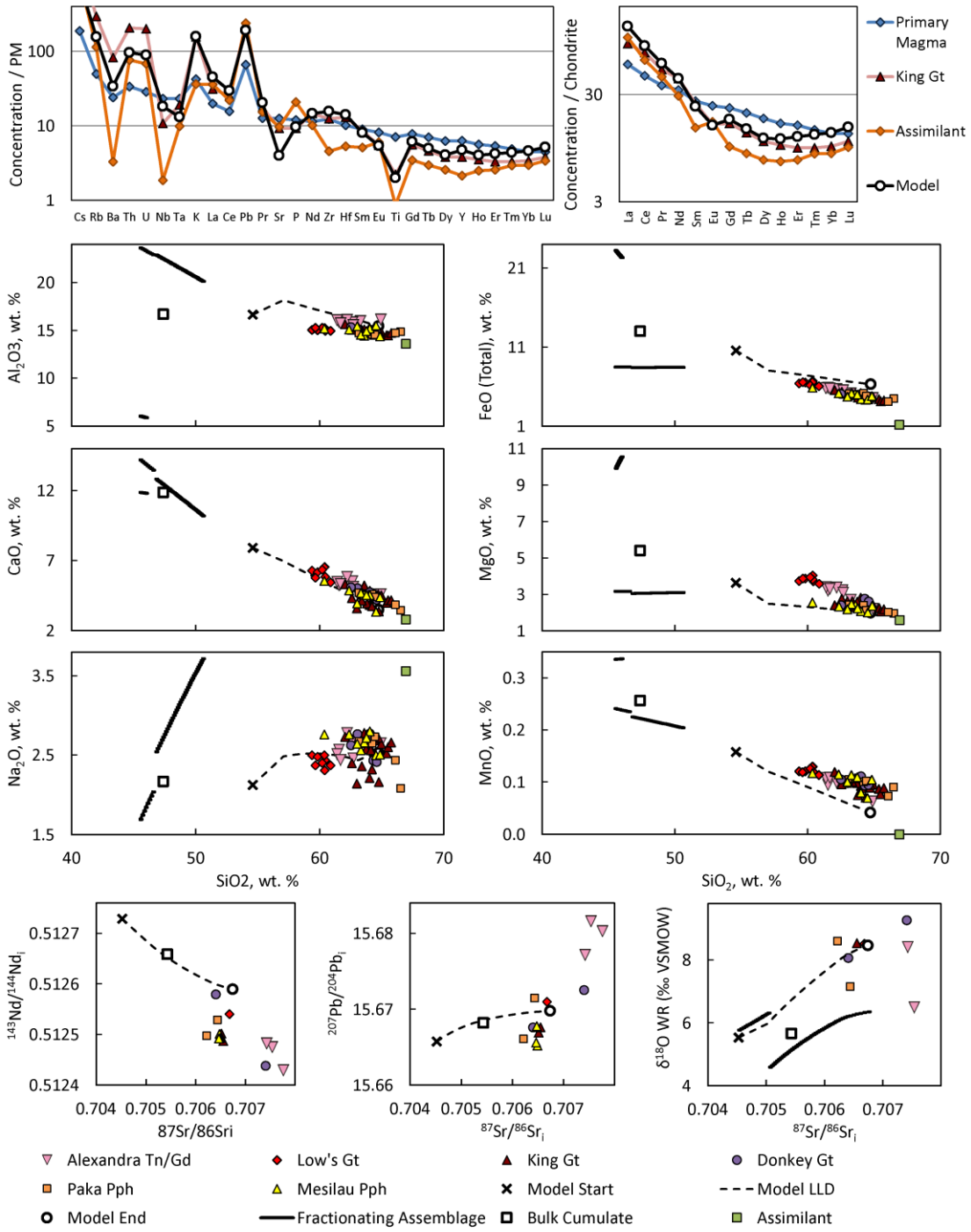

796

797 Fig. 12. Compositional comparison (isotopes, trace elements and selected major
798 elements) of the EME-AFC King Granite model end values, liquid line of descent
799 (LLD), fractionating assemblage and bulk cumulate with the primary magma (2.1%
800 Na_2O and 2.5% K_2O; Model 3 in Fig. 11), partially melted xenolith and partially
801 melted BPQ assimilant (used respectively for trace and major elements) and King

802 Granite target composition. Normalising values from Sun and McDonough (1989).

803 Abbreviations as in Fig. 1.

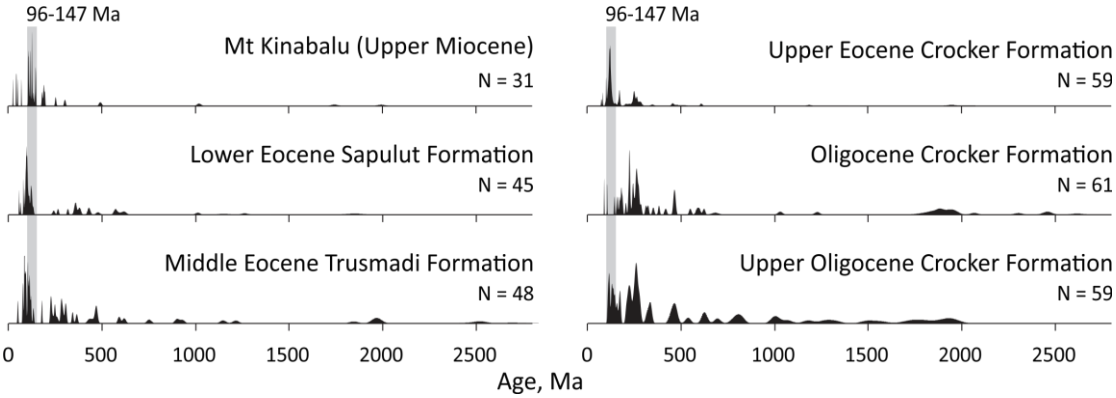

804

805 Fig. 13. Probability density plots of $^{206}Pb/^{238}U$ inherited zircon ages from Mt Kinabalu

806 (Cottam *et al.*, 2010) and $^{206}Pb/^{238}U$ detrital zircon ages from the principal

807 sedimentary units of Sabah: the Eocene Sapulut and Trusmadi Formations and the

808 Eocene-Oligocene units of the Crocker Formation (van Hattum *et al.*, 2013).

809

Table 1. Whole rock Major and trace element data from Mt Kinabalu. * Major element data from Sperber (2009).

Table 2. Isotopic data from Mt Kinabalu. *Whole rock $\delta^{18}O$ calculated from hornblende $\delta^{18}O$ as detailed in the text.

Table 3. Two-component major element partition coefficients determined from experimental data (Grove *et al.*, 2003; Alonso-Perez *et al.*, 2009; Nandedkar *et al.*, 2014), including the values used for EME-AFC modelling of Mt Kinabalu.

Table 4. Fractionating phases, parameters and outputs of the EME-AFC modelling of the compositional range of the Alexandra Tonalite/Granodiorite, the Low's Granite and the King Granite.

Lat.	6.0728	6.0784	6.0763	6.0756	6.0790	6.0818	6.0767	6.0712	6.1235	6.0831	6.1224	6.0310	6.0750	6.0768	6.0788
Long.	116.5570	116.5513	116.5502	116.5537	116.5500	116.5492	116.5490	116.5533	116.5720	116.5538	116.5738	116.7251	116.5587	116.5571	116.5570
Height, m	4030	3827	3929	3959	3803	3684.11	3991.24	3891.51	2586	3945	0	0	4096	3947	3847
	Alex. Gd	Alex. Gd	Alex. Gd	Alex. Gd	Alex. Gd	Alex. Gd	Alex. Gd	Alex. Gd	Low's Gt	Low's Gt	Low's Gt	Low's Gt	Low's Gt	Low's Gt	Low's Gt
	CS016	CS021	CS022	CS023	CS036	A042	A047	A054	CS077	A046	A218	SBK121	CS018	CS019	CS020
(wt%)															
SiO_2	63.26	61.53	62.62	62.19	62.68	64.91	61.38	61.67	60.88	60.21	59.65	60.40	60.45	60.39	59.38
TiO_2	0.65	0.68	0.66	0.72	0.66	0.54	0.63	0.66	0.63	0.66	0.68	0.71	0.67	0.69	0.67
Al_2O_3	15.99	15.87	15.85	16.10	15.56	16.13	16.07	15.75	14.96	15.29	15.29	15.25	14.96	15.13	15.07
FeO_{TOT}	5.14	5.84	5.42	5.70	5.53	4.54	5.81	5.79	6.07	6.19	6.56	6.74	6.44	6.56	6.43
MnO	0.10	0.10	0.10	0.10	0.10	0.06	0.11	0.11	0.11	0.13	0.12	0.13	0.12	0.13	0.12
MgO	2.72	3.23	3.24	3.39	3.10	2.23	3.40	3.32	3.59	3.94	3.87	4.05	3.72	3.83	3.74
CaO	4.73	5.28	5.54	5.84	5.14	4.61	5.49	5.35	5.47	6.36	5.80	6.57	5.87	6.55	6.30
Na_2O	2.66	2.57	2.69	2.78	2.46	2.65	2.52	2.44	2.37	2.40	2.37	2.31	2.44	2.50	2.50
K_2O	3.30	2.64	2.55	2.02	2.67	2.89	2.31	2.59	3.68	2.69	3.44	2.73	3.62	2.99	3.34
P_2O_5	0.18	0.18	0.19	0.20	0.18	0.17	0.18	0.18	0.26	0.24	0.28	0.30	0.27	0.29	0.27
Total	99.30	99.44	99.46	99.67	99.53	99.90	107.60	99.42	99.75	99.84	100.02	99.94	99.28	99.79	99.12
LOI	0.73	0.87	0.57	1.00	0.84	0.66	1.06	0.92	1.05	1.05	1.23	1.24	0.50	0.93	0.58
ppm															
Ta	0.78	0.71	0.66	0.68	0.66	0.82	0.64	0.67	0.58	0.62	0.63	0.66	0.62	0.60	0.70
Sc	14.20	22.04	17.91	21.34	21.54	12.94	20.47	20.45	21.35	21.79	22.11	17.88	17.97	18.30	17.12
V	100.34	187.45	142.53	166.38	167.06	101.80	176.00	173.00	184.49	188.30	201.10	151.50	151.41	155.76	151.54
Cr	42.20	58.87	50.84	56.45	57.66	35.12	62.96	65.45	75.68	92.40	82.55	62.35	61.20	63.80	60.12
Ga	13.97	17.75	14.50	17.62	17.67	17.68	17.94	17.71	16.65	16.93	17.67	13.74	13.81	14.17	14.05
Co	10.89	15.47	13.14	15.11	15.29	10.71	16.32	16.01	20.25	20.39	20.47	16.33	16.95	17.04	16.47
Ni	24.91	16.65	18.99	15.39	14.60	11.44	17.18	16.82	18.23	22.27	20.15	13.11	14.60	13.89	13.14
Cu	3.73	35.34	12.23	5.12	23.57	7.39	22.66	17.64	43.11	28.37	52.02	1052.8	29.28	62.40	38.56
Zn	40.50	48.60	44.49	34.90	50.79	38.10	54.04	59.54	50.76	59.52	54.50	71.75	45.11	45.67	48.48
Cs	9.17	9.45	9.41	7.71	8.25	9.57	9.71	9.00	11.32	5.46	11.75	9.12	11.57	8.93	9.73
Rb	103.26	102.26	86.82	92.40	98.63	107.30	83.80	93.55	117.35	68.08	119.50	74.43	107.97	90.63	83.41
Ba	770.96	901.42	924.83	925.12	890.96	834.60	816.00	865.50	847.28	856.00	854.30	977.93	1010.8	867.50	863.25
Sr	193.66	239.28	214.07	249.52	248.24	255.50	247.10	257.90	273.97	310.30	300.70	243.30	238.73	252.41	266.49
Zr	171.00	143.40	136.20	154.30	136.60	167.20	143.30	148.60	125.60	141.20	126.90	130.20	111.00	120.40	142.70
Hf	4.51	4.14	3.68	4.23	3.64	4.50	3.97	4.05	3.42	3.78	3.44	3.53	3.16	3.34	3.93
Th	11.58	10.09	8.86	9.87	10.22	11.53	8.92	12.42	12.17	10.20	8.98	9.58	10.01	10.14	10.00
U	2.12	2.20	1.87	2.10	1.86	2.39	2.02	2.49	2.48	2.30	2.24	2.44	2.24	2.26	2.27
Pb	11.20	7.18	8.98	4.58	7.14	10.59	9.42	9.94	12.95	13.22	12.43	12.22	11.73	11.47	13.71
Nb	10.13	8.80	8.07	8.56	8.40	10.10	8.24	8.65	7.03	7.81	14.89	7.99	7.09	7.81	8.04
Y	22.52	20.87	19.88	20.27	20.08	18.52	21.26	21.19	17.84	19.71	20.40	20.37	17.88	19.79	19.44
La	24.34	21.00	20.17	21.33	20.53	21.73	19.17	19.94	17.32	18.41	22.52	19.26	19.90	20.12	19.73
Ce	53.38	49.06	40.01	44.14	42.32	53.30	42.83	45.92	37.70	43.87	40.88	40.60	39.31	41.47	44.03
Pr	5.97	5.52	4.16	4.60	4.39	5.82	5.27	5.10	4.03	4.82	5.12	4.67	4.19	4.80	4.87
Nd	24.07	22.08	19.01	20.75	19.73	23.51	19.03	21.24	18.46	20.01	17.74	19.63	19.01	20.40	20.63
Sm	4.59	4.36	3.91	4.14	4.01	4.44	4.28	4.20	3.76	4.07	4.23	4.09	3.87	4.18	4.22
Eu	0.98	1.01	0.96	0.97	0.93	0.99	1.03	1.03	0.98	0.99	1.13	1.01	0.97	1.00	1.03
Gd	4.20	4.11	3.63	3.86	3.74	3.67	4.17	3.88	3.50	3.73	4.04	3.84	3.62	3.82	3.93
Tb	0.60	0.62	0.56	0.60	0.59	0.55	0.61	0.60	0.53	0.56	0.60	0.55	0.54	0.58	0.57
Dy	3.55	3.60	3.29	3.47	3.35	3.09	3.60	3.52	3.10	3.24	3.31	3.23	3.15	3.28	3.28
Ho	0.73	0.74	0.67	0.71	0.67	0.62	0.75	0.71	0.61	0.64	0.65	0.66	0.62	0.66	0.66
Er	1.96	1.94	1.85	1.94	1.83	1.67	2.05	1.95	1.67	1.78	1.76	1.78	1.70	1.80	1.79
Tm	0.28	0.28	0.31	0.34	0.31	0.26	0.24	0.31	0.29	0.27	0.13	0.25	0.29	0.27	0.27
Yb	2.12	2.09	1.92	2.00	1.91	1.75	2.14	2.05	1.70	1.83	1.91	1.93	1.74	1.84	1.82
Lu	0.34	0.36	0.31	0.32	0.32	0.28	0.35	0.34	0.29	0.30	0.31	0.33	0.29	0.30	0.31

826

827 Table 1. Whole rock Major and trace element data from Mt Kinabalu. *Major element

828 data from Sperber (2009).

829

Lat.	6.1214	6.0733	6.0640	6.0640	6.0766	6.0788	6.0943	6.0741	6.0589	6.0729	6.0705	6.0684	6.0740	6.0738	6.0791	6.0800
Long.	116.5776	116.5575	116.5670	116.5704	116.5758	116.5810	116.5807	116.5790	116.5653	116.5704	116.5703	116.5704	116.6282	116.6168	116.5259	116.5298
Height, m	3025	0	3577	3460	3918	3769	3657	4007	3241.9	3488.96	3611.29	3767.98	3007.82	3126.3	1886.21	2150.33
	Low's Gt	King Gt	King Gt	King Gt	King Gt	King Gt	King Gt	King Gt	King Gt	King Gt	King Gt	King Gt	King Gt	King Gt	King Gt	King Gt
	CS081	SBK123	CS011 c	CS028	CS031	CS066	CS069	CS072	A089c	A128	A129	A131	A236	A237	A282	A285
(wt%)																
SiO_2	59.84	64.04	64.40	64.39	63.59	62.06	64.01	64.96	64.12	64.72	65.53	65.77	63.39	63.01	64.77	62.59
TiO_2	0.67	0.53	0.52	0.52	0.52	0.53	0.55	0.47	0.50	0.47	0.41	0.44	0.51	0.52	0.48	0.54
Al_2O_3	15.02	14.81	14.53	15.13	15.12	15.63	15.30	14.84	14.70	14.88	14.48	14.74	15.06	15.34	14.97	15.06
FeO_{TOT}	6.52	5.04	4.35	4.68	4.89	5.57	5.22	4.64	4.94	4.74	4.14	4.27	5.10	5.10	4.75	5.34
MnO	0.12	0.09	0.07	0.09	0.10	0.12	0.11	0.10	0.09	0.09	0.08	0.09	0.10	0.10	0.10	0.10
MgO	3.87	2.81	2.74	2.60	2.32	2.41	2.82	2.39	2.54	2.40	2.08	2.19	2.64	2.64	2.41	2.78
CaO	6.20	4.86	4.68	4.39	5.25	5.32	3.85	4.53	4.61	4.60	4.18	4.18	4.15	3.60	3.39	4.34
Na_2O	2.48	2.61	2.71	2.69	2.78	2.73	2.21	2.64	2.56	2.72	2.60	2.66	2.36	2.14	2.16	2.40
K_2O	3.40	3.89	4.28	4.65	3.86	4.95	4.51	4.29	4.52	4.40	4.57	4.58	4.34	4.56	4.73	4.50
P_2O_5	0.28	0.20	0.23	0.24	0.26	0.29	0.23	0.21	0.22	0.21	0.18	0.18	0.23	0.24	0.20	0.24
Total	99.75	99.96	99.64	99.90	99.24	100.23	99.39	100.09	99.90	100.32	99.32	100.05	100.02	100.15	100.30	100.03
LOI	0.61	0.52	0.64	1.11	0.77	0.36	1.87	0.49	0.54	0.56	0.60	0.47	1.57	2.33	1.81	1.55
ppm																
Ta	0.70	0.78	0.96	0.82	0.96	0.75	0.81	0.81	0.75	0.64	0.69	0.82	0.73	0.75	0.78	0.68
Sc	25.38	16.83	17.04	13.84	14.24	14.64	15.98	15.56	15.81	14.28	12.29	12.75	15.73	16.03	14.67	17.29
V	211.19	141.75	145.30	115.51	128.08	132.57	112.15	128.95	134.80	123.80	110.70	111.30	134.50	132.90	125.40	147.00
Cr	86.95	58.35	53.81	39.79	31.06	26.75	81.18	46.97	45.75	41.78	37.58	38.94	47.08	47.23	43.60	51.33
Ga	17.65	15.71	16.45	12.25	13.66	13.95	11.85	15.66	16.09	15.76	15.33	15.49	16.10	15.91	16.15	16.56
Co	23.59	15.37	12.67	12.58	10.94	12.59	13.63	14.30	13.29	14.05	12.07	12.74	14.72	15.20	13.62	15.01
Ni	21.19	14.41	12.77	8.78	5.70	4.66	42.73	12.31	12.27	11.72	10.25	11.86	12.83	12.77	11.87	13.62
Cu	59.84	41.01	30.50	21.90	5.70	40.82	8.18	33.83	56.78	26.90	22.19	9.50	18.93	14.43	11.64	16.00
Zn	58.31	41.66	43.02	44.54	30.50	34.30	80.77	44.58	43.56	39.86	32.78	40.89	48.25	49.98	44.44	43.56
Cs	10.08	17.65	12.97	15.04	5.56	9.66	10.34	13.63	18.75	8.65	9.55	17.32	8.88	10.45	13.48	9.93
Rb	119.46	140.99	165.50	166.03	97.37	153.96	144.18	160.97	188.70	158.30	174.60	197.10	155.20	173.70	187.40	167.30
Ba	912.61	883.93	605.60	865.41	677.98	586.81	825.67	661.57	650.50	680.00	623.10	644.00	653.50	720.80	576.50	700.20
Sr	314.28	261.09	283.90	181.39	295.92	293.62	164.05	283.56	296.70	314.10	293.20	288.70	256.80	232.80	195.70	271.00
Zr	140.00	132.80	149.80	132.70	155.10	205.90	137.50	120.10	127.60	135.70	126.70	128.60	140.30	136.10	140.10	142.20
Hf	3.92	3.65	4.28	3.77	4.38	5.63	3.84	3.33	3.45	3.63	3.42	3.68	3.81	3.83	4.03	3.91
Th	10.14	17.71	23.69	13.14	26.48	19.45	14.86	15.58	42.61	21.66	15.98	18.84	18.69	17.14	17.57	9.04
U	2.44	3.83	5.20	3.17	5.18	4.99	3.30	3.57	5.14	4.47	3.87	5.19	3.78	3.50	4.23	2.74
Pb	12.79	13.04	18.06	25.07	13.03	21.02	23.53	19.13	21.76	16.64	16.14	20.48	18.89	20.58	16.74	17.85
Nb	8.01	7.64	8.71	8.76	9.99	8.31	8.79	7.89	8.01	7.17	6.77	7.54	7.86	8.06	7.73	7.57
Y	19.82	15.39	19.69	18.72	23.68	19.73	20.74	15.90	17.37	16.30	15.03	14.99	18.18	18.35	17.36	18.14
La	26.52	16.58	19.70	23.10	39.21	23.75	22.24	20.21	18.95	19.85	17.88	21.09	19.84	23.63	21.35	17.06
Ce	44.20	37.63	50.81	42.66	73.18	51.13	47.99	37.50	37.62	38.99	34.07	38.23	43.21	49.15	45.40	40.82
Pr	5.11	4.07	5.51	4.41	7.69	5.91	5.54	3.88	4.67	4.42	4.05	4.51	4.85	5.21	4.91	4.72
Nd	20.81	16.15	22.13	20.19	30.22	23.75	22.37	17.11	16.30	18.30	13.79	14.96	20.19	21.50	19.84	19.69
Sm	4.22	3.15	4.38	4.11	5.63	4.90	4.49	3.39	3.79	3.66	3.22	3.38	4.03	4.13	3.80	3.98
Eu	1.03	0.78	1.07	0.90	1.16	1.13	0.98	0.87	0.96	0.91	0.87	0.88	0.97	1.00	0.92	0.97
Gd	3.88	2.84	3.88	3.58	4.66	4.25	3.97	2.98	3.42	3.18	2.83	3.10	3.40	3.62	3.33	3.56
Tb	0.57	0.40	0.60	0.55	0.71	0.60	0.57	0.45	0.49	0.48	0.41	0.44	0.51	0.54	0.50	0.52
Dy	3.34	2.45	3.28	3.15	3.90	3.44	3.34	2.57	2.87	2.70	2.37	2.58	2.97	3.08	2.79	3.01
Ho	0.67	0.48	0.67	0.61	0.78	0.68	0.68	0.52	0.56	0.54	0.48	0.51	0.60	0.62	0.58	0.61
Er	1.78	1.29	1.84	1.73	2.13	1.85	1.80	1.43	1.56	1.49	1.30	1.36	1.65	1.73	1.58	1.61
Tm	0.24	0.19	0.29	0.29	0.34	0.27	0.25	0.24	0.16	0.24	0.11	0.12	0.26	0.27	0.25	0.26
Yb	1.94	1.47	1.95	1.85	2.26	2.11	1.96	1.54	1.67	1.63	1.48	1.55	1.74	1.83	1.68	1.76
Lu	0.32	0.25	0.33	0.30	0.36	0.37	0.33	0.26	0.27	0.26	0.24	0.25	0.28	0.30	0.28	0.29

830

831 Table 1. (cont.)

Lat.	6.0798	6.0880	6.0705	6.0747	6.0819	6.0665	6.0565	6.0514	6.0555	6.0638	6.0734	6.0747	6.0819	6.0665	6.0565
Long.	116.5350	116.5780	116.5647	116.5697	116.5780	116.5640	116.5646	116.5639	116.5647	116.5739	116.5844	116.5697	116.5780	116.5640	116.5646
Height, m	2443.77	3767	3946.06	3389.22	3805.71	3755.96	0	0	3096	3508.18	3888.38	3389.22	3805.71	3755.96	0
	King Gt	Donkey Gt	Donkey Gt	Donkey Gt	Donkey Gt	Donkey Gt	Paka Pph	Paka Pph	Paka Pph	Paka Pph	Paka Pph	Donkey Gt	Donkey Gt	Donkey Gt	Paka Pph
	A286	CS033	A093	A127	A145	A079	SBK128	SBK130	CS027	A155	A162	A127	A145	A079	SBK128
(wt%)															
SiO_2	64.22	64.06	64.63	63.08	62.56	64.34	64.25	66.53	66.11	64.46	63.17	63.08	62.56	64.34	64.25
TiO_2	0.49	0.48	0.54	0.49	0.52	0.57	0.52	0.45	0.45	0.47	0.50	0.49	0.52	0.57	0.52
Al_2O_3	15.10	14.76	14.70	15.16	15.32	14.89	14.55	14.84	14.71	14.49	14.70	15.16	15.32	14.89	14.55
FeO_{TOT}	4.78	5.04	4.72	4.95	5.03	4.85	5.14	4.48	4.08	4.76	5.09	4.95	5.03	4.85	5.14
MnO	0.10	0.11	0.09	0.10	0.10	0.09	0.10	0.09	0.07	0.10	0.10	0.10	0.10	0.09	0.10
MgO	2.47	2.17	2.60	2.30	2.41	2.75	2.40	1.96	2.02	2.13	2.44	2.30	2.41	2.75	2.40
CaO	3.76	4.73	4.21	5.01	5.08	4.38	4.60	3.45	3.84	4.41	4.70	5.01	5.08	4.38	4.60
Na_2O	2.32	2.77	2.41	2.76	2.62	2.43	2.65	2.08	2.43	2.73	2.67	2.76	2.62	2.43	2.65
K_2O	4.54	5.03	4.29	4.39	4.84	4.26	4.98	4.97	5.30	4.87	4.92	4.39	4.84	4.26	4.98
P_2O_5	0.21	0.25	0.22	0.24	0.25	0.23	0.27	0.22	0.22	0.24	0.25	0.24	0.25	0.23	0.27
Total	100.10	100.25	99.71	99.36	99.80	99.93	100.03	99.57	100.07	99.56	99.59	99.36	99.80	99.93	100.03
LOI	1.59	0.29	0.76	0.33	0.51	0.59	0.20	1.38	0.38	0.38	0.47	0.33	0.51	0.59	0.20
ppm															
Ta	0.68	0.92	0.83	0.62	0.75	0.83	1.01	1.11	0.90	0.82	0.88	0.62	0.75	0.83	1.01
Sc	15.47	15.30	16.01	14.74	15.22	16.11	11.49	9.98	12.89	13.89	15.35	14.74	15.22	16.11	11.49
V	125.80	139.25	117.00	139.30	144.40	119.10	109.92	95.34	122.22	138.00	152.50	139.30	144.40	119.10	109.92
Cr	44.68	27.98	47.09	35.63	35.96	50.97	24.65	22.29	31.93	32.81	43.18	35.63	35.96	50.97	24.65
Ga	15.92	15.96	16.57	16.61	17.40	16.77	13.15	13.15	14.79	15.77	16.46	16.61	17.40	16.77	13.15
Co	14.33	14.41	12.50	14.04	14.02	12.68	9.20	9.55	14.23	13.87	15.40	14.04	14.02	12.68	9.20
Ni	11.87	7.88	11.29	10.00	10.09	12.36	6.99	5.18	9.78	9.73	12.53	10.00	10.09	12.36	6.99
Cu	14.52	23.21	16.69	26.39	31.78	26.31	105.34	47.95	143.70	35.64	44.41	26.39	31.78	26.31	105.34
Zn	42.65	44.63	59.55	40.96	32.48	58.49	26.23	30.63	31.11	39.30	36.46	40.96	32.48	58.49	26.23
Cs	12.66	12.25	17.95	8.15	7.87	13.81	7.90	11.14	10.74	16.77	12.16	8.15	7.87	13.81	7.90
Rb	189.50	202.78	178.60	150.80	182.00	177.10	175.83	170.41	233.82	224.00	221.80	150.80	182.00	177.10	175.83
Ba	679.00	567.97	561.90	646.80	675.60	591.90	511.13	469.77	441.85	463.70	579.50	646.80	675.60	591.90	511.13
Sr	244.30	328.89	302.80	360.20	361.20	322.80	270.88	209.50	300.51	344.00	377.30	360.20	361.20	322.80	270.88
Zr	130.40	134.70	161.60	138.90	154.30	179.90	124.30	130.90	117.80	118.60	135.90	138.90	154.30	179.90	124.30
Hf	3.67	4.07	4.62	3.80	4.19	4.77	3.89	4.09	3.52	3.43	4.05	3.80	4.19	4.77	3.89
Th	16.97	24.40	20.90	17.42	17.01	14.69	27.64	30.93	28.21	10.54	26.72	17.42	17.01	14.69	27.64
U	4.00	6.14	4.10	3.66	2.73	3.14	6.46	5.80	4.82	3.94	6.30	3.66	2.73	3.14	6.46
Pb	16.41	20.45	24.38	16.22	13.65	21.75	25.55	23.71	17.83	19.31	22.55	16.22	13.65	21.75	25.55
Nb	7.57	8.80	9.76	7.49	7.59	10.29	9.00	9.74	8.19	8.33	8.85	7.49	7.59	10.29	9.00
Y	16.82	20.18	21.73	20.01	19.24	22.27	18.11	22.11	18.19	18.70	18.91	20.01	19.24	22.27	18.11
La	20.48	22.70	26.84	17.73	19.40	24.07	19.98	30.43	28.31	17.42	24.71	17.73	19.40	24.07	19.98
Ce	46.25	47.97	60.79	44.21	41.95	54.53	48.93	57.24	54.11	36.46	55.81	44.21	41.95	54.53	48.93
Pr	4.87	5.62	6.67	5.08	5.17	6.63	5.85	6.70	5.55	4.81	6.23	5.08	5.17	6.63	5.85
Nd	19.83	22.74	27.12	22.00	18.05	23.68	24.13	26.84	24.28	17.98	25.34	22.00	18.05	23.68	24.13
Sm	3.82	4.60	5.24	4.38	4.21	5.22	4.97	5.14	4.45	4.37	4.97	4.38	4.21	5.22	4.97
Eu	0.93	1.03	1.13	1.09	1.08	1.21	1.13	1.16	1.00	1.07	1.13	1.09	1.08	1.21	1.13
Gd	3.30	3.94	4.45	3.84	3.83	4.63	4.16	4.21	3.67	3.94	4.00	3.84	3.83	4.63	4.16
Tb	0.49	0.55	0.66	0.57	0.55	0.66	0.56	0.60	0.52	0.51	0.56	0.57	0.55	0.66	0.56
Dy	2.77	3.04	3.73	3.23	3.12	3.77	3.13	3.37	2.90	3.00	3.14	3.23	3.12	3.77	3.13
Ho	0.56	0.62	0.76	0.67	0.62	0.75	0.63	0.68	0.59	0.59	0.63	0.67	0.62	0.75	0.63
Er	1.54	1.74	2.08	1.80	1.67	2.14	1.69	1.87	1.66	1.62	1.71	1.80	1.67	2.14	1.69
Tm	0.25	0.25	0.32	0.29	0.16	0.24	0.25	0.27	0.29	0.14	0.28	0.29	0.16	0.24	0.25
Yb	1.65	2.05	2.20	1.88	1.90	2.26	1.93	2.19	1.83	1.82	1.90	1.88	1.90	2.26	1.93
Lu	0.27	0.34	0.36	0.31	0.30	0.36	0.33	0.37	0.31	0.29	0.30	0.31	0.30	0.36	0.33

832

833 Table 1. (cont.)

Lat.	6.0514	6.0555	6.0638	6.0734	6.0665	6.0814	6.0793	6.0800	6.0723	6.0494	6.0733	6.0595	6.0595	6.132023	6.03124	6.070546
Long.	116.5639	116.5647	116.5739	116.5844	116.5815	116.5867	116.5909	116.5999	116.6012	116.5891	116.6143	116.5936	116.5940	116.5698	116.5483	116.5642
Height, m	0	3096	3508.18	3888.38	3769	3332	3513	3133	3413	2715	3134	2393	2393	2239	1874	3968
	Paka Pph	Paka Pph	Paka Pph	Paka Pph	Mes Pph	Mes Pph	Mes Pph	Mes Pph	Mes Pph	Mes Pph	Mes Pph	Mes Pph	Mes Pph	Quartzite	Sst	Xenolith
	SBK130	CS027	A155	A162	A152	A167	A170	A172	A173	A190	A241	CS055	CS056	A221	A291	A098
(wt%)																
SiO_2	66.53	66.11	64.46	63.17	63.61	64.87	63.32	62.37	63.01	60.38	63.77	64.04	64.54	77.95	83.81	83.42
TiO_2	0.45	0.45	0.47	0.50	0.51	0.48	0.52	0.52	0.47	0.53	0.49	0.48	0.50	0.51	0.46	0.20
Al_2O_3	14.84	14.71	14.49	14.70	14.45	14.36	14.55	15.10	15.43	15.18	14.91	15.19	15.52	10.62	8.40	8.08
FeO_{TOT}	4.48	4.08	4.76	5.09	5.12	4.80	5.16	5.18	4.72	5.87	5.01	4.40	4.37	4.15	1.75	1.26
MnO	0.09	0.07	0.10	0.10	0.11	0.11	0.11	0.11	0.10	0.12	0.11	0.08	0.07	0.05	0.01	0.01
MgO	1.96	2.02	2.13	2.44	2.41	2.38	2.48	2.35	2.19	2.58	2.24	2.10	2.03	1.59	0.64	0.99
CaO	3.45	3.84	4.41	4.70	4.60	4.40	4.70	4.88	3.96	5.58	4.56	4.54	3.37	0.03	-0.05	1.90
Na_2O	2.08	2.43	2.73	2.67	2.66	2.51	2.56	2.76	2.64	2.76	2.72	2.80	2.50	0.21	1.79	1.37
K_2O	4.97	5.30	4.87	4.92	4.82	4.70	4.81	4.80	5.13	4.82	4.71	4.67	6.16	2.03	1.03	1.49
P_2O_5	0.22	0.22	0.24	0.25	0.25	0.23	0.25	0.26	0.23	0.31	0.24	0.22	0.24	0.06	0.07	0.04
Total	99.57	100.07	99.56	99.59	99.49	100.06	99.55	99.41	99.43	99.21	99.96	100.08	99.79	99.87	99.70	99.88
LOI	1.38	0.38	0.38	0.47	0.38	0.69	0.50	0.50	1.02	0.43	0.64	1.06	1.68	2.21	1.60	
ppm																
Ta	1.11	0.90	0.82	0.88	1.00	0.81	0.76	0.77	0.59	0.45	0.80	0.59	0.61	0.75	0.56	0.31
Sc	9.98	12.89	13.89	15.35	15.17	14.47	15.93	14.90	14.12	16.24	14.88	14.02	10.44	8.39	4.94	3.77
V	95.34	122.22	138.00	152.50	146.10	139.40	153.50	151.30	134.20	177.70	145.70	135.70	92.37	67.99	49.69	29.08
Cr	22.29	31.93	32.81	43.18	41.46	44.92	49.28	37.89	39.13	28.72	35.15	36.54	20.51	51.51	29.31	25.95
Ga	13.15	14.79	15.77	16.46	16.72	15.97	16.07	17.40	16.70	17.01	16.87	16.62	13.17	11.48	8.32	8.00
Co	9.55	14.23	13.87	15.40	15.38	14.46	15.63	15.27	13.94	17.80	14.80	14.21	8.93	7.79	2.04	4.82
Ni	5.18	9.78	9.73	12.53	12.38	11.87	13.34	11.06	11.20	9.39	10.52	10.00	2.43	21.91	7.25	34.96
Cu	47.95	143.70	35.64	44.41	51.80	206.10	1.96	57.62	81.57	54.91	53.99	262.78	347.06	19.44	7.20	6.37
Zn	30.63	31.11	39.30	36.46	46.21	42.32	44.33	49.67	50.75	49.10	52.40	35.21	19.91	44.64	32.70	10.61
Cs	11.14	10.74	16.77	12.16	12.99	12.39	9.55	12.42	10.94	8.89	13.41	7.34	8.36	6.79	3.77	9.03
Rb	170.41	233.82	224.00	221.80	225.00	203.00	216.60	209.60	216.90	182.20	219.70	238.44	221.90	96.26	46.23	111.50
Ba	469.77	441.85	463.70	579.50	446.30	368.30	460.90	560.10	610.70	729.00	446.10	379.01	450.60	201.90	141.20	137.40
Sr	209.50	300.51	344.00	377.30	343.20	335.40	365.50	425.20	410.10	438.30	386.30	419.03	334.79	38.71	35.01	133.90
Zr	130.90	117.80	118.60	135.90	114.60	133.70	120.50	135.70	117.20	134.50	118.40	107.00	99.45	230.80	274.80	24.11
Hf	4.09	3.52	3.43	4.05	3.34	3.76	3.42	3.86	3.28	3.48	3.50	3.03	2.83	6.08	7.13	0.67
Th	30.93	28.21	10.54	26.72	19.12	15.11	28.49	25.16	21.88	22.20	28.05	26.15	26.17	9.16	8.74	5.12
U	5.80	4.82	3.94	6.30	6.48	3.92	5.01	4.53	4.41	3.61	5.72	5.20	4.95	2.08	2.01	1.15
Pb	23.71	17.83	19.31	22.55	24.41	20.32	23.42	23.94	26.45	20.60	25.46	19.64	22.82	6.23	7.96	7.59
Nb	9.74	8.19	8.33	8.85	9.32	8.02	7.94	8.65	7.04	5.82	8.38	6.75	6.69	8.85	6.47	3.25
Y	22.11	18.19	18.70	18.91	20.02	17.93	16.92	19.62	16.67	13.81	19.24	14.53	13.87	19.29	20.23	10.26
La	30.43	28.31	17.42	24.71	21.62	25.69	24.77	25.95	25.01	20.53	27.37	20.97	26.07	20.54	22.52	14.53
Ce	57.24	54.11	36.46	55.81	46.64	49.55	51.36	57.97	51.57	40.90	58.16	47.20	46.94	42.96	39.21	27.94
Pr	6.70	5.55	4.81	6.23	5.92	5.99	5.69	6.54	5.76	4.48	6.59	5.04	4.96	5.27	5.48	3.43
Nd	26.84	24.28	17.98	25.34	21.11	21.10	23.72	27.44	23.72	18.91	27.50	22.24	22.09	19.69	21.09	12.53
Sm	5.14	4.45	4.37	4.97	4.83	4.75	4.66	5.35	4.65	3.72	5.30	4.38	4.07	3.87	4.37	2.31
Eu	1.16	1.00	1.07	1.13	1.11	1.08	1.08	1.19	1.17	1.08	1.17	1.08	1.07	0.60	0.92	0.67
Gd	4.21	3.67	3.94	4.00	4.31	4.31	3.74	4.19	3.69	3.07	4.14	3.44	3.15	3.57	4.39	2.02
Tb	0.60	0.52	0.51	0.56	0.57	0.56	0.52	0.59	0.52	0.43	0.57	0.46	0.44	0.58	0.64	0.31
Dy	3.37	2.90	3.00	3.14	3.12	3.06	2.86	3.18	2.81	2.31	3.20	2.53	2.36	3.32	3.42	1.71
Ho	0.68	0.59	0.59	0.63	0.62	0.59	0.57	0.62	0.57	0.45	0.64	0.51	0.46	0.70	0.70	0.33
Er	1.87	1.66	1.62	1.71	1.69	1.59	1.53	1.71	1.53	1.21	1.71	1.33	1.27	1.96	1.90	0.89
Tm	0.27	0.29	0.14	0.28	0.15	0.14	0.24	0.28	0.24	0.19	0.27	0.23	0.22	0.32	0.30	0.14
Yb	2.19	1.83	1.82	1.90	1.91	1.81	1.60	1.88	1.63	1.26	1.84	1.44	1.33	2.07	1.94	0.84
Lu	0.37	0.31	0.29	0.30	0.31	0.30	0.27	0.31	0.28	0.22	0.30	0.24	0.23	0.35	0.33	0.13

834

835 Table 1. (cont.)

836

												$\delta^{18}O_{V\text{-}SMOW}$ (‰)						
Lithology	Sample	$^{87}Sr/^{86}Sr_m$	2SE	$^{143}ND/^{144}Nd_m$	2SE	$^{206}Pb/^{204}Pb_m$	2SE	$^{207}Pb/^{204}Pb_m$	2SE	$^{208}Pb/^{204}Pb_m$	2SE	Hornblende	SD	Quartz	SD	Biotite	SD	Whole Rock $\delta^{18}O$ (‰)*
Alexandra Tn/Gd	A042	0.707888	11	0.512435	08	18.7761	06	15.6811	07	39.0200	34							
Alexandra Tn/Gd	A047	0.707640	10	0.512482	07	18.7729	11	15.6823	10	39.0192	43	4.8	0.4	8.3	0.1	-1.3	0.4	6.9
Alexandra Tn/Gd	A049	0.707939	07	0.512449	11	18.7763	06	15.6791	07	39.0151	31	8.2	0.14	9.8	0.3			9.1
Alexandra Tn/Gd	A054	0.707536	18	0.512488	04	18.7732	12	15.6780	12	39.0094	31	6.6	0.0	10.3	0.1	4.9	0.3	8.4
Low's Gt	A046											7.0	0.4					8.3
Low's Gt	A218	0.706805	18	0.512548	06	18.7477	09	15.6716	09	38.9647	30	7.2	0.1	10.2	0.1	5.9	0.4	8.5
Low's Gt	SBK122	0.706989	09	0.512505	08	18.7463	06	15.6698	08	38.9574	34							
King Gt	A236	0.706702	12	0.512508	08	18.7387	08	15.6676	08	38.9488	47							
King Gt	A282	0.706849	08	0.512493	10	18.7397	08	15.6685	07	38.9460	27	7.0	0.1	9.8	0.4	0.3	0.3	8.5
Donkey Gt	A093	0.707595	16	0.512443	09	18.7518	12	15.6731	12	38.9766	41	8.1	0.9	10.0	0.1			9.3
Donkey Gt	A096											7.5	0.1					9.0
Donkey Gt	A127	0.706542	17	0.512584	04	18.7366	10	15.6683	09	38.9451	32	6.6	0.3	9.6	0.1			8.1
Paka Pph	A162	0.706644	09	0.512503	10	18.7363	06	15.6670	08	38.9371	35	6.8	0.0	10.1	0.1			8.6
Paka Pph	A290b	0.706938	11	0.512500	08	18.7264	06	15.6635	07	38.9163	27							
Paka Pph	CS027	0.706682	16	0.512533	05	18.7474	08	15.6724	07	38.9699	27	5.4	0.8					7.2
Mesilau Pph	A172	0.706642	10	0.512499	10	18.7337	07	15.6659	08	38.9351	32							
Mesilau Pph	A198	0.706462	08	0.512526	08	18.7288	10	15.6669	10	38.9306	33	7.2	0.4	9.4	0.4			8.4
Mesilau Pph	A239											6.7	0.2					7.9
Mesilau Pph	A241	0.706646	09	0.512498	07	18.7373	08	15.6664	07	38.9409	29							
Mesilau Pph	CS055	0.706653	09	0.512507	07	18.7417	08	15.6687	08	38.9491	32							
Xenolith	A098	0.710785	17	0.512259	09	18.7482	15	15.6729	14	38.9582	45							
Quartzite	A221	0.715460	72	0.512387	27	18.8302	11	15.6966	11	39.1173	34							
Quartzite	A291	0.713415	75	0.512413	06	18.8495	10	15.6903	09	39.1089	26							

Table 2. Isotopic data from Mt Kinabalu. *Whole rock $\delta^{18}O$ calculated from hornblende $\delta^{18}O$ as detailed in the text.

Two-Component	Partition Coefficients	Min	Max	Mean	SD	n	Kinabalu value
Plagioclase	$(Al^{Plag} \times Si^{Liq}) / (Si^{Plag} \times Al^{Liq})$	1.79	4.20	2.46	0.51	36	2.46
Pl. (52-57 % SiO_2)	$(Al^{Plag} \times Si^{Liq}) / (Si^{Plag} \times Al^{Liq})$	1.79	2.22	2.01	0.18	5	2.01
Pl. (57-63 % SiO_2)	$(Al^{Plag} \times Si^{Liq}) / (Si^{Plag} \times Al^{Liq})$	1.90	2.85	2.31	0.31	16	2.31
Pl. (>63 % SiO_2)	$(Al^{Plag} \times Si^{Liq}) / (Si^{Plag} \times Al^{Liq})$	2.05	4.20	2.80	0.58	14	2.80
Plagioclase	$(K^{Plag} \times Na^{Liq}) / (Na^{Plag} \times K^{Liq})$	0.03	0.19	0.09	0.04	36	0.09
Hornblende	$(Fe^{Hbl} \times Mg^{Liq}) / (Mg^{Hbl} \times Fe^{Liq})$	0.23	0.53	0.36	0.07	28	0.25
Hornblende	$(Al^{Hbl} \times Si^{Liq}) / (Si^{Hbl} \times Al^{Liq})$	0.26	1.60	1.13	0.27	28	0.60
Clinopyroxene	$(Fe^{Cpx} \times Mg^{Liq}) / (Mg^{Cpx} \times Fe^{Liq})$	0.20	0.51	0.28	0.07	23	0.28
Clinopyroxene	$(Al^{Cpx} \times Si^{Liq}) / (Si^{Cpx} \times Al^{Liq})$	0.12	0.68	0.27	0.18	23	0.27
Orthopyroxene	$(Fe^{Opx} \times Mg^{Liq}) / (Mg^{Opx} \times Fe^{Liq})$	0.20	0.53	0.28	0.08	15	0.28
Orthopyroxene	$(Al^{Opx} \times Si^{Liq}) / (Si^{Opx} \times Al^{Liq})$	0.07	0.52	0.19	0.16	15	0.19
Olivine	$(Fe^{Ol} \times Mg^{Liq}) / (Mg^{Ol} \times Fe^{Liq})$	0.24	0.33	0.28	0.03	14	0.28
Biotite	$(Al^{Bt} \times Si^{Liq}) / (Si^{Bt} \times Al^{Liq})$	2.52	2.52	2.52		1	2.52
Garnet	$(Fe^{Cpx} \times Mg^{Liq}) / (Mg^{Cpx} \times Fe^{Liq})$	0.60	1.59	0.97	0.28	16	0.97

Table 3. Two-component major element partition coefficients determined from experimental data (Grove *et al.*, 2003; Alonso-Perez *et al.*, 2008; Nandedkar *et al.*, 2014).

Fractionating phases	Melt SiO_2, wt.%			Bulk Cumulate, %			
	52-57	57-63	>63	Alexandra	Low's	King	Other units
Ol							
Cpx	42			11.7-14.9	19.4-23.9	13.8-17.3	13.1-21.1
Opx	42			11.7-14.9	19.4-23.9	13.8-17.3	13.1-21.1
Hbl		30	30	19.2-21.5	12.8-16.0	17.5-20.0	14.8-20.5
Pl	11	65	65	45.5-49.7	34.0-39.7	42.4-46.9	37.6-47.8
Kfs							
Bt							
Ap	0.5	0.5	0.5	0.5	0.5	0.5	0.5
Mag	1.5	1.5	1.5	1.5	1.5	1.5	1.5
Ilm	3.5	3.5	3.5	3.5	3.5	3.5	3.5
Zrn		0.02	0.02	0.01	0.01	0.01	0.01
Rt							
Grt							
F				0.59-0.73	0.72-0.78	0.54-0.66	0.5-0.74
r, $M_{assimilated}/M_{crystallised}$				0.56-0.72	0.65-0.73	0.4-0.57	0.36-0.66
ρ, total $M_{assimilated}/M^0_{melt}$				0.22-0.29	0.16-0.21	0.23-0.25	0.2-0.25

848

849 Table 4. Fractionating phases, parameters and outputs of the EME-AFC modelling of

850 the Alexandra Tonalite/Granodiorite, the Low's Granite and the King Granite.

851

852